The Thesis Committee for Rita Abdo Bitar Nehme
Certifies that this is the approved version of the following thesis:

Geochemistry and High-Resolution Chemostratigraphy of the Haynesville Formation, East Texas

APPROVED BY
SUPERVISING COMMITTEE:

Harold Rowe, Co-supervisor

William Fisher, Co-supervisor

Charles Kerans

Geochemistry and High-Resolution Chemostratigraphy of the Haynesville Formation, East Texas

by

Rita Abdo Bitar Nehme, B.S.

Thesis

Presented to the Faculty of the Graduate School of

The University of Texas at Austin

in Partial Fulfillment

of the Requirements

for the Degree of

Master of Science in Geological Sciences

The University of Texas at Austin

May 2015

Dedication

To my parents Abdo and Salam,

and

To my sisters Michele, Greta and Romy.

Acknowledgements

I would like to extend my gratitude to my supervisors, Dr. Harry Rowe for his continuous support and great passion for science and research, and Dr. William Fisher for giving me the opportunity to come to UT and his guidance. I would also like to thank Dr. Charles Kerans for taking the time to read my thesis and providing his valuable comments, and David DeGroot for his great assistance during my graduate studies.

I would like to extend my appreciation to the Bureau of Economic Geology staff, especially Michael Nieto and Nathan Ivicic for their help and constant positive attitude.

I want to thank my Texas 4000 family for their inspiration, for some of the best moments of my life, and for motivating me to live to make this world a better place.

I also want to thank Weam Al-Awar for being an incredible friend, Christina Karam for always being my buddy, Zeina Wafa for her beautiful presence in my life, Carine C for being the best bannout, Mayra Martinez for her amazing spirit, Elena Kassab la sopapillas de mi corazon, Tito Ontess Kassab, the wonderful Abdallah, Afif, George, Chris, Felipe, Mario, Franco and all the habibis. Their friendship is very dear to my heart.

I want to thank Majd Helal for being my partner in crime, always pushing me forward and believing in me. To the precious thing we have, the amazing adventure we are building and all the dreams we share.

I am beyond grateful for my father Abdo who taught me to be proud of who I am and fight for what I want, my mom Salam for always making everything better with her amazing person and unconditional love, my sister Michele who is my best source of laughter and my motivation to be as smart as her, my sister Greta who inspires me to be brave and dream big, and my sister Romy who brings joy to my life with her loving heart and beautiful self. I would not be the person I am today without them.

Abstract

Geochemistry and High-Resolution Chemostratigraphy of the Haynesville Formation, East Texas

Rita Abdo Bitar Nehme, M.S. Geo. Sci.

The University of Texas at Austin, 2015

Supervisor: Harold Rowe and William Fisher

The Upper Jurassic Haynesville Formation of East Texas and Louisiana is an organic-rich calcareous mudrock that is Kimmeridgian in age. It underlies the less calcareous Bossier Shale, and it overlies the Smackover Formation limestone. The Haynesville has low permeability, but a relative high porosity, compared to other mudrock formations.

Mudrocks are the most common sedimentary rock and some of the most challenging to study, analyze and understand. Despite having a homogeneous appearance on a macroscopic scale, mudrocks often have high variability in facies and composition on the microscopic scale and elemental level. Many studies and methods have been developed to identify facies and stratigraphic variations in mudrocks. A complete understanding of these variations is valuable to comprehend paleoenvironments, paleoclimate and paleoceanographic conditions. Mudrocks studies are also beneficial to shale exploration because these formations, which have a high hydrocarbon content, can be targeted by oil and gas companies for exploration and production.

Geochemical methods, chemostratigraphy in particular, will be used in this thesis to complement core description, petrophysical studies and sedimentological studies. This thesis focuses on acquiring chemostratigraphic data from X-Ray Fluorescence (XRF) and X-Ray Diffraction (XRD) measurements to identify elemental and mineralogical variations in the T. W. George core, from the Haynesville Formation in Harrison County, Texas. The data are linked to core description and are analyzed using Hierarchical Cluster Analysis (HCA) to acquire a better understanding of the paleoceanographic conditions and depositional environments that controlled the sediment deposition of the Haynesville Formation. The Haynesville Formation comprises a Ca-rich lower Haynesville, a more Ca-rich upper Haynesville, and underlies the Si-rich and Ca-poor Bossier. The dominant condition during deposition is anoxic/euxinic in the lower Haynesville becoming dysoxic in the upper Haynesville and more oxygenated in the Bossier Formation. The greenhouse climate of the Late Jurassic led to the deposition of strata yielding petroleum source rocks such as the Haynesville Formation that today have great economic value. Thus, studying the Haynesville has both academic and economic importance.

Table of Contents

List of Tables x

List of Figures xi

Chapter 1: Introduction 1

1. Study Objectives 1
2. Late Jurassic Paleoclimate 2
3. Previous Work on the Haynesville Formation 6
   - 3.1. Sequence Stratigraphy and Depositional Setting 7
   - 3.2. Petrography of the Haynesville 9
   - 3.3. Biota of the Haynesville 10
   - 3.4. Economic Analysis of the Haynesville 10
   - 3.5. Chemostratigraphy of the Haynesville 11
4. Geochemical Proxies and Relationships 13

Chapter 2: Methods 25

1. XRF 25
2. Bambino Hardness 26
3. Hierarchal Cluster Analysis 28

Chapter 3: Results 30

1. Core Description 30
2. XRD Mineralogy 35
3. Total Organic Carbon 35
4. XRF Cross-Plots: Detrital Hosted Elements 38
5. XRF Cross-Plots: Carbonate Hosted Elements 40
6. Chemostratigraphic Variations of Elements with Depth 41
7. Ca-Si-Al Ternery Diagram 48
8. Bulk Elemental Mineralogy Trends 49
9. Elemental Proxies of TOC 51
10. Hierarchal Cluster Analysis 52

Chapter 4: Discussion 65
1. Relative Sedimentary Contribution.....65
1.1. Detrital Influx.....65
1.2. Calcareous Phase Analysis 67
2. Depositional Environment of the Haynesville.....69
3. Paleo-Productivity of the Haynesville 71
4. Sequence Stratigraphy of the Haynesville 73
4.1. Highstand 75
4.2. Lowstand.....76
4.3. Maximum Flooding Surface (MFS).....76
4.4. HCA Sequence Boundary Interpretations.....77
Chapter 5: Conclusions 79
Bibliography 81

List of Tables

Table 1: Major elements and their significance in a depositional environment context. 22

Table 2: Trace elements and their significance in a depositional environment context. 23

Table 3: T. W. George core study analysis. 28

Table 4 (a): HCA elemental ranking (Clusters 1-7) 59

Table 4 (b): HCA elemental ranking (Clusters 8-15) 60

Table 5: Summary of clusters with labels based on their chemical distribution 64

List of Figures

Figure 1: Regional map of Texas and Louisiana showing the major shale plays, including the Haynesville. Also shown is the T. W. George core locality in Harrison County, East Texas. 2

Figure 2: Map of continents during the Late Jurassic (Blakey, and Ranney, 2014) 5

Figure 3: Relative variation of CO2 during the Late Jurassic and Early Cretaceous, plotted using C-isotope data from Weissert and Erba (2004).....6

Figure 4: Upper Jurassic stratigraphic section of East Texas showing formations and lithology from shelf to basin, systems tracts (LST, TST, HST ¼ lowstand, transgressive, highstand systems tracts), maximum flooding surface (MFS), and supersequence boundaries (SB SS1, 2, 3) (modified after Goldhammer, 1998; Hammes and Frébourg, 2011; and Hammes et al., 2011). 9

Figure 5: Set-up of Bruker XRF Tracer- SD used for X-ray fluorescence elemental data collection. 26

Figure 6: Stratigraphic column of the T. W. George core based on core description on a macroscopic scale. Core pictures depths in Figure 14 are indicated by red squares 31

Figure 7: High resolution core scans from the T. W. George core. Note: Images have been modified for contrast. Core depth can be found on Figure 17. 32

Figure 8: (a) Mineralogic variation (b) TOC variation. 37

Figure 9: Cross-plots of percentages of detrital elements including %Si, %Ti and %K vs. %Al, as well as %Ca (representing calcite) vs. %Al and the two detrital trace elements Ga and Th (in ppm) vs. %Al.....39
Figure 10: Cross-plot of iron vs. aluminum. 39
Figure 11: Cross-plots of elemental content %Mg, %Fe, %Mn, and Sr (ppm) (carbonate elements) vs. Ca, as well as %K and %Si (detrital elements) vs. %Ca. 41
Figure 12: Chemostratigraphy of major elements and Si/Al ratio 45
Figure 13: Chemostratigraphy of trace elements.....46
Figure 14: Chemostratigraphy of detrital elements and sulfur.....47
Figure 15: Ternary diagram representing the Ca-Al-Si relationship of the T. W. George core from the East Texas Basin (Brumsack, 1989). Red data points are out-of-range values.....49
Figure 16: Bulk Elemental-Mineralogy Trends 50
Figure 17: Elemental proxies of TOC 51
Figure 18: HCA heat map generated by Spotfire software showing chemical distribution of the 15 different clusters.....58
Figure 19: Cluster stratigraphy graph showing the distribution of the 15 clusters along the depth of the core.....61
Figure 20: Cluster stratigraphy graph with ordered clusters showing the formation's evolution 62
Figure 21: Hierarchical Cluster Analysis graph aligned with the chemical stratigraphy of P, Ca, Zn and Mo.....63

Chapter 1: Introduction

1. Study Objectives

The objective of this thesis is to analyze the depositional environment of the Haynesville Formation and to describe the paleoceanographic characteristics and conditions that were dominant during the time of deposition.

The Haynesville is one of the most targeted mudrock formations in the United States. Mudrocks constitute about a third of the sedimentary record (Schieber and Zimmerle, 1998). Studying mudrocks can provide insight on depositional settings, paleoceanography, paleoproductivity and paleoclimate in different geological times. Mudrocks are challenging to study because of their homogeneity and fine-grained character. Core description and analysis of the T. W. George core, Haynesville Formation, from a macroscopic point of view reveals a relatively homogeneous formation. Geochemical studies using elemental and mineralogical data were a necessary and complementary scientific approach to study the variations in mudrock formations. Hierarchical Cluster Analysis (HCA) divides the core into chemical facies that cannot be analyzed by chemostratigraphic studies alone. The results and interpretation presented in this thesis have both economic value, because mudrocks are source rocks for petroleum exploration, and academic value, because these results indicate the environmental, climatic and oceanographic conditions that existed during the Kimmeridgian in what is today known as the East Texas Basin.

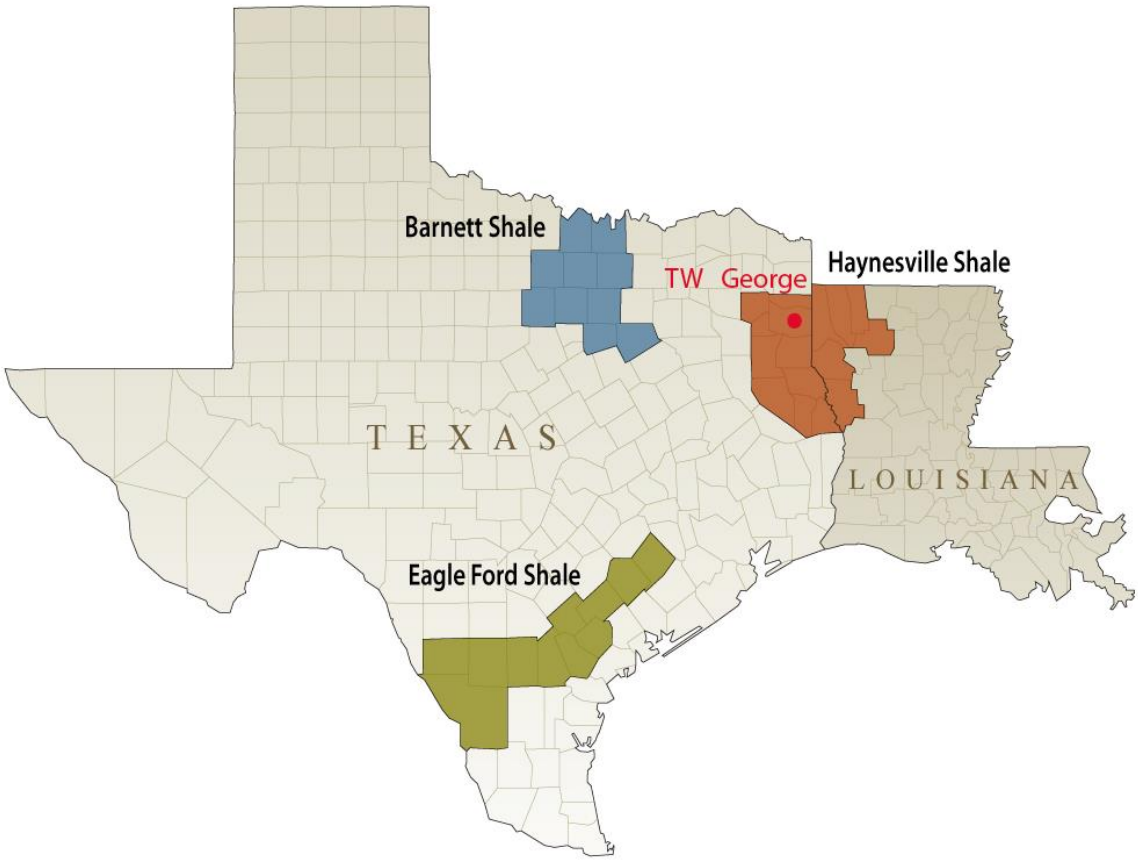

Figure 1: Regional map of Texas and Louisiana showing the major shale plays, including the Haynesville. Also shown is the T. W. George core locality in Harrison County, East Texas.

2. LATE JURASSIC PALEOCLIMATE

The Haynesville Formation was deposited during the Late Jurassic Kimmeridgian Epoch. Climates in the Jurassic and Cretaceous are generally considered to have been warmer than modern climate (Hallam, 1993; Parrish, 1993; Zakharov et al., 2005). Polar ice sheets were unlikely in the Mesozoic because of the high overall temperatures. Coral reefs grew 10˚ of latitude north and south (Sellwood and Valdes, 2006). Dense forests formed close to the poles, where months-long daylight occurred in the summers and months-long darkness occurred in the winters (Sellwood and Valdes, 2006). Warm

temperatures dominated ocean depths (8˚C) and the Earth (6˚C higher than modern days), leading to higher atmospheric humidity levels and a more enhanced hydrological cycle (Sellwood and Valdes, 2006). The Mid-Triassic time interval was probably the most arid climate in Earth's history. Higher atmospheric humidity dominated at the beginning of the Jurassic; during the Late Jurassic, the climate changed on a global scale, changing from humid to more arid climate conditions (Hallam et al., 1993; Parrish, 1993). Plate tectonic activity, especially the opening of the Atlantic Ocean and the Indian Ocean, led to eustatic changes during the Late Jurassic (Hallam, 2001). High volcanic activity caused relatively high concentrations of atmospheric carbon dioxide (Berner, 1994).Warm climatic conditions extended into the Mid-Cretaceous, considered to be the warmest period of the Mesozoic (Valdes and Sellwood, 1992; Zakharov et al., 2005).

At low and mid-latitudes the climate conditions were tropical-subtropical, characterized by seasonal rainfall (Valdes and Sellwood, 1992; Hallam et al., 1993). At high latitudes the climate was temperate, characterized by arid conditions. According to interpretations made from stable oxygen isotope analysis, the temperatures during most of the Cretaceous were found to be between 25 and 30 °C, and bottom-water temperatures were approximately 15°C, an indication of warm polar waters (Valdes and Sellwood, 1992; Hallam et al., 1993).

The Kimmeridgian and Tithonian of the Late Jurassic are significant times in the division of the supercontinent Pangea, which had assembled during the Late Paleozoic and Early Mesozoic, into Gondwana and Laurasia (Parrish, 1993; Demko and Parrish, 1998). Starting during the Triassic and during the Jurassic, rifting events occurred along the Ouachita thrust belt. This led to extension and breakup of Pangea. It also resulted in sea-floor spreading and thermal subsiding of the lithosphere (Goldhammer and Johnson, 1999; Steinhoff et al., 2011). The breakup of Pangea occurred through the reestablishment and

formation of new seaway connections when North America separated from Gondwana. The rift system opening the proto-Indian ocean split Gondwana into North and South continents. This led to the establishment of two connections by the late Tithonian: the Tethys Sea and the Panthalassa Ocean (Ross et al., 1992). Another important characteristic of this period was the high overall sea level that occurred. It has been hypothesized that Late Jurassic atmospheric circulation patterns were more zonal than the Early and Middle Jurassic meridional patterns, characteristic of Pangean monsoon (Hallam et al., 1993; Parrish, 1993; Demco and Parrish, 1997).

Haynesville strata were deposited during the formation of the East Texas Basin. In the early Oxfordian, a divergent margin formed, leading to the opening of the Gulf of Mexico and movement of salt when North and South America separated. On a global scale during the Late Jurassic, the predominant depositional system at low latitudes was evaporites, and at mid- to high latitudes the systems were palustrine (Rees et al., 2004). This difference is due to a transition from drier conditions at the equator to wetter conditions at the poles (Parrish, 1993).

Figure 2: Map of continents during the Late Jurassic (Blakey, and Ranney, 2014)

Many researchers used general circulation models (GCMs) to reconstruct the climate of the Mesozoic era (Sellwood and Valdes, 2006), the Jurassic (Moore et al., 1992), the Late Jurassic (Kimmeridgian) and the mid-Cretaceous epoch (Cenomanian) (Valdes and Sellwood, 1997; Price et al., 2007). When modelled and correlated with paleoclimate reconstruction from sedimentary rocks, the Late Jurassic was confirmed to be a time of elevated greenhouse forcing (Hallam, 1985; Moore et al., 1992; Weiserret and Elba, 2004) and of high atmospheric CO_2 (~1850 ppm) (Berner, 1990, 1992; Hallam et al., 1991; Weiserret and Elba, 2004; Figure 3)

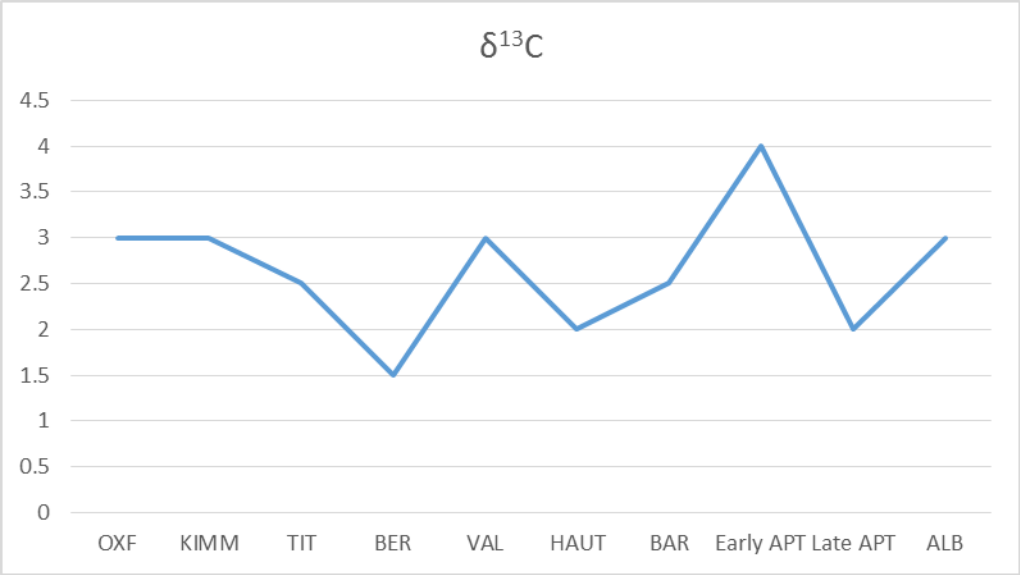

Figure 3: Relative variation of CO2 during the Late Jurassic and Early Cretaceous, plotted using C-isotope data from Weissert and Erba (2004)

In their high-resolution model of the Late Jurassic, Valdes and Sellwood (1992) [13]surmised an absence of polar ice cover and the occurrence of some glaciation at high latitudes. The climatic condition was arid over the southwestern North American continent and seasonally arid over southern Europe (Parrish, 1993). Despite the absence of ice, temperatures dropped to below zero for much of the winter in Siberia and southeastern Gondwanaland (Valdes and Sellwood, 1992).

3. Previous Work on the Haynesville Formation

Many research studies of the Haynesville Formation used different approaches on different levels: petrophysics (Butler and Dix, 2009; Hammes, 2010), burial and thermal history (Nunn, 2012), sequence stratigraphy and sedimentology (Hammes, 2009; Cicero et al., 2010; Hammes, 2010), depositional systems (Cicero et al., 2010, Steinhoff et al., 2011), paleoclimate and paleoceanography (Mainali, 2011). These studies hold both scientific and economic value (Piper and Calvert, 2009).

3.1.Sequence Stratigraphy and Depositional Setting

The occurrence of black shale in the stratigraphic record is usually linked to marine transgressions (Arthur and Sageman, 1994) because the organic carbon-rich facies mainly accumulate during these major sequence-stratigraphic episodes. Thus, many researchers, including Cicero et al. (2010), Hammes and Frébourg (2011) and Nunn (2012), focused on the sequence-stratigraphic aspect of the Haynesville. One of the main characteristics of the Haynesville sequence stratigraphy is the occurrence of both retrogradational and progradational facies at the same time (Cicero et al., 2010). The Haynesville Formation strata were deposited during a 2nd-order transgressive systems tract (TST) (Goldhammer, 1998). This tract included proximal back-stepping ramp carbonates and distal marine shales (McLean et al., 1999; Goldhammer and Johnson, 2001; Cicero et al., 2010; Hammes et al., 2011). The shale onlaps retrogradational carbonates and basement highs (McLean et al., 1999; Hammes et al., 2011). It is capped by a 2nd-order maximum flooding surface (MFS) (Cicero et al., 2010; Hammes et al., 2011). Above the Haynesville Formation and after the 2nd-order MFS, the Bossier shale and local sandstones prograde basinward and downlap on the MFS. They grade upward and into the fluvio-deltaic sandstones of the Cotton Valley Group, a highstand systems tract (HST). The restricted environments that dominate the Bossier are characterized by the development of distal organic-rich facies, making it a productive gas-shale (Cicero et al., 2010; Hammes, 2011).

The Haynesville Formation was deposited during worldwide transgression with the maximum flooding surface (MFS) occurring at the Haynesville-Bossier boundary in the Tithonian (Goldhammer, 1999; Hammes, 2011). The depositional systems of the Upper Jurassic Haynesville and Bossier shale-gas plays, located in the northwestern Gulf of Mexico Basin, are mainly produced from organic-rich, marine transgressive highstand

mudrocks within mixed carbonate-clastic strata (Arthur and Sageman, 1994; Hammes, 2009; Hammes et al., 2010, 2011).

The deposition of highly organic versus non-organic lithologies and the deposition of siliciclastic-dominated versus carbonate-dominated lithologies are influenced by basin restriction (Arthur and Sageman, 2005) and partitioning due to several preexisting basement highs in the south and carbonate platforms in the northwest and west (Arthur and Sageman, 1994; Hammes et al., 2011). During Haynesville deposition, siliciclastic input mainly originated from the north and northeast, with a development of carbonate facies to the south and to the west (Goldhammer, 1998; Hammes et al., 2011).

The sequence-stratigraphic packaging of the Haynesville was based on mass wasting events, depositional settings and sedimentary features. It is difficult and problematic to apply sequence-stratigraphic concepts because of facies having distal setting, below storm-wave base deposition, sediment of pelagic source and the different sedimentary processes involved (Frébourg et al., 2013). The upper Haynesville is an example of that, having been deposited with an internally complex sedimentary geometry; there is no display of internal cyclicity, which makes it hard to distinguish the position of the second-order MFS (Hammes et al., 2011; Frébourg et al., 2013).

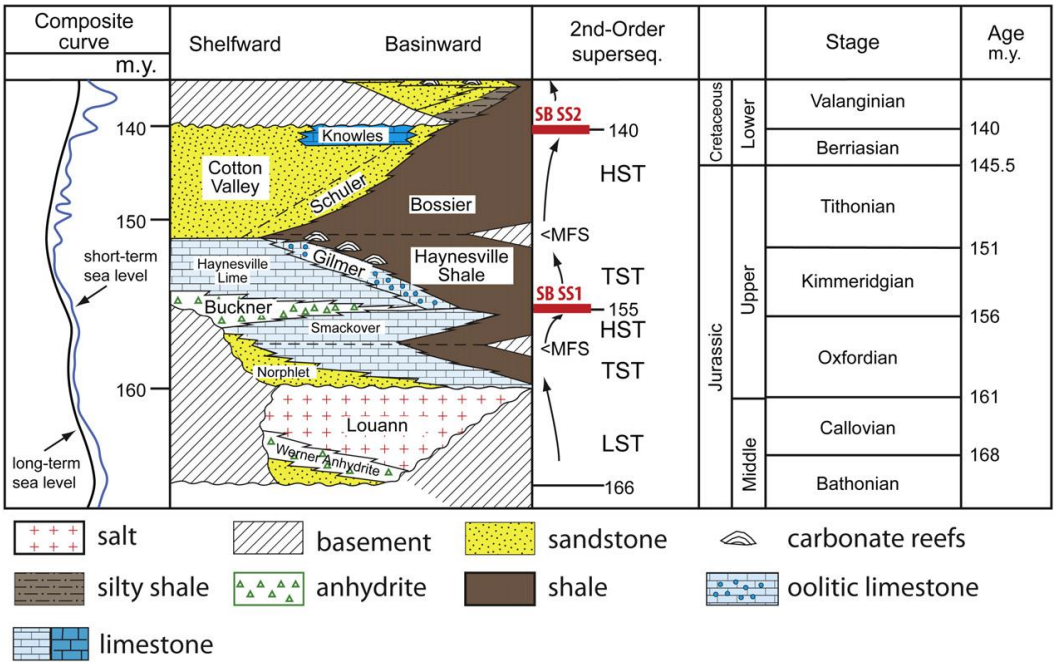

Figure 4: Upper Jurassic stratigraphic section of East Texas showing formations and lithology from shelf to basin, systems tracts (LST, TST, HST ¼ lowstand, transgressive, highstand systems tracts), maximum flooding surface (MFS), and supersequence boundaries (SB SS1, 2, 3) (modified after Goldhammer, 1998; Hammes and Frébourg, 2011; and Hammes et al., 2011).

3.2.Petrography of the Haynesville

Petrographic analyses and macroscopic interpretations were conducted on the Haynesville and Bossier and were linked to the geochemical data acquired by Hammes et al. (2011). This type of study led to the identification and interpretation of different petrographic facies and sequences based on detailed core description and thin-section analyses. The three main facies that were identified on the basis of mineralogy, fabric, biota, and texture are:

- Unlaminated peloidal mudstone
- Laminated peloidal calcareous or siliceous mudstone
- Bioturbated calcareous or siliceous mudstone

3.3.Biota of the Haynesville

Biotic events during the Kimmeridgian were dominated by paleotemperatures that dropped from the Early Kimmeridgian to the Late Kimmeridgian, leading to a decrease in the generic diversity of benthos. The Early Kimmeridgian, a warmer time interval, was dominated by the thermophile Trigoniidae bivalve family, whereas the Late Kimmeridgian, which was cooler, had the least diversified benthos (Zakharov et al., 2005).

The Haynesville biota is characterized by a settlement of benthic bivalve communities and of bioturbating organisms during deposition that happened below storm-wave base. Conditions were dysoxic, periodically oscillating to more anoxic on the seafloor (Kauffman, 1990; Aller, 1994, Leckie, 2002). The scattered fauna is mainly of planktonic origin (Leckie, 2002).

3.4.Economic Analysis of the Haynesville

From an economic point of view, the techniques in this thesis are helpful for shale-gas evaluation and assessment, which is of great interest to the petroleum industry. The Late Jurassic time, especially the Kimmeridgian and Tithonian, was one of the most prolific times for organic-rich source-rock deposition (Klemme, 1994; Ewing, 2001).The deposition stretched from the Gulf of Mexico to the Tethys across the proto-Atlantic (Moore et al., 1995; Hammes et al., 2011). The Haynesville and Bossier intervals developed into one of the most prolific shale-gas plays in North America, with estimated recoverable resources in the hundreds of trillions of cubic feet of gas (Williams, 2009; Wang and Hammes, 2010). Typically, the best shale-gas reservoirs are found in the most distal, anoxic and high-organic settings (Loucks and Ruppel, 2007), which makes the Haynesville a shale-gas play targeted by researchers and petroleum companies. Some of the main values showing the economic importance of the Haynesville are: The TOC ranges from 1 to 5.5%, with an average thermal maturity of 1.43% Ro (Hammes et al., 2011).

Some the main economic values from the Middle Bossier (interval: 14,000 ft; 4600 m) are: The TOC ranges from 1 to 8.5%, with an average thermal maturity of 2.06% Ro (Hammes et al., 2011). By 2010, the estimated recoverable reserves of the Haynesville were up to 100 Tcf (Spain and Anderson, 2010). For exploration, it is very important to have a deeper and more detailed understanding of the variations in lithology, stratigraphy, geochemistry and fauna across the basin.

When mudrock formations are studied for petroleum exploration, the formations might look homogeneous on a macroscopic scale, but they are very heterogeneous and complex on a microscopic scale, both mineralogically and geochemically. Geochemical studies are necessary to understand and explore mudrocks. Chemostratigraphic correlations and the understanding of these correlations in shale plays can be a very useful and significant tool for exploration.

3.5.Chemostratigraphy of the Haynesville

Geochemistry provides a link between solid Earth and its hydrosphere, biosphere, cryosphere, atmosphere and climate, which are mediated by short and long-term biogeochemical cycles (Sageman et al., 2005). Geochemistry is the main approach used in this thesis to link stratigraphic framework to paleoclimate (Pearce et al., 2005; Ratcliffe et al., 2010) and provenance (Ratcliffe et al., 2007; Wright et al., 2010).

Chemostratigraphic studies complement lithostratigraphic studies using a quantitative approach. Chemostratigraphy uses trace chemical elements, major chemical elements and mineralogy to characterize and correlate strata. Very often, lithostratigraphic units have different geochemical signatures; this makes chemostratigraphy a quantitative means of differentiating lithostratigraphic units that cannot be studied macroscopically (Tribovillard et al., 2005; Sano et al., 2013).

Detrital sedimentary rocks are characterized by four stages of formation (Sageman et al., 2005). Geochemical data can be acquired from the four different stages of detrital sedimentation. The first stage is the provenance, which is the source site of the sediment. Factors dominating that source are tectonic activity, bedrock sedimentology and climate control. The second stage is the transport of the sediments from the source. In this stage the dominant factors include the medium, the gradient and the distance of transport. The third stage is the site of deposition. This includes the chemical, physical and biological processes governing the site and controlling the sediment deposition and early burial. The final stage is the later burial. Factors dominating this stage are the diagenetic processes and controls that alter the sediment characteristics. Sediments are left with geochemical signatures that can be acquired at any of those stages, yielding information about paleoenvironmental conditions such as oxygen and carbon dioxide level in the atmosphere and paleoceanographic conditions including redox state and salinity (Sageman et al., 2005). To do this analysis, we use geochemical proxies. Sageman et al. (2005) provided a method for linking the processes of detrital, biogenic and authigenic accumulation in fine-grained hemipelagic settings; that model incorporates both a conceptual representation and methods using geochemical proxies.

Knowledge of the modern environment is extrapolated to proxy-based interpretations of ancient strata. Detrital sediments preserve a wide range of proxies that clarify the process and conditions of the sediment formation, transport, deposition and burial, especially if an integrated multi-proxy approach is used. Chemical proxies and their use are elaborated in the following sections.

4. GEOCHEMICAL PROXIES AND RELATIONSHIPS

To link chemostratigraphic data to paleoclimate and paleoceanography requires understanding and applying different elemental proxies. Geochemical proxies were used to study different shale plays, such as the Stark Shales of the North American midcontinent (Algeo and Maynard, 2004, 2009), Upper Devonian Ohio Shale of eastern North America (Rimmer, 2004; Algeo and Maynard, 2009), the Mississippian Barnett Shale (Rowe et al., 2008) and the Haynesville Formation (Hammes et al., 2011; Sano et al., 2013; Frébourg et al., 2013).

The concentration of a given element in a sedimentary deposit depends on its content in the three different phases: the continents, the sea floor and the water column. Sedimentary geochemistry is an important tool for reconstructing climatic and oceanographic changes and for understanding how the composition of major and trace elements of the sea-floor deposits provides information on terrestrial climate and ocean conditions (Calvert and Pedersen, 2007).

Patterns of trace-metal variations in sediments not only give information about benthic redox conditions (Algeo and Maynard, 2004) but also they can give insight into hydrographic characteristics and water-mass properties (Algeo and Manyard, 2009). Paleoceanographic systems and features are assessed by the evaluation of aqueous concentrations of trace metals, renewal time of the deep watermass and the short-term and long-term changes in the trace-metal inventories of seawater. In restricted anoxic marine systems, chemostratigraphic studies and trace-metal/TOC ratios can indicate the degree of watermass restriction and estimates of deep water renewal times. Sediment trace-metal ratios may provide evidence of the chemical evolution of basinal deep-water in response to differential rates of trace-metal removal to the sediment. The degree of deep-water restriction in silled basins is generally controlled by eustatic variations, with higher sea

levels resulting in lesser watermass restriction and lower sea levels resulting in greater watermass restriction. Short-term (million-year scale) drawdown of the trace-metal inventory of seawater has occurred simultaneously with oceanic anoxic events, resulting in high rates of trace-metal removal to widespread anoxic facies. In contrast, long-term (eon-scale) changes in trace-metal composition of seawater have occurred in response to changes in atmospheric–oceanic redox conditions and their effects on trace-metal cycling (Algeo and Rowe, 2012).

Trace elements can be used to estimate paleoceanic chemistry, condition and water mass restriction. Both modern oceans and paleo-oceans have been studied to show the relationships between these paleoceanographic conditions and trace elements (Algeo and Rowe, 2012). When examining variation patterns of trace-metals/TOC, such as Mo/TOC for example, we can determine the dominant factor controlling the accumulation of trace metals and whether it is hydrographic or redox controlled (Rowe et al., 2008; Algeo and Rowe, 2012). Degree of Pyritization (DOP) is another geochemical measurement that serves as a redox proxy. Evaluation of elemental concentrations and normalization of elemental data are both essential for geochemical interpretation (Calvert and Pedersen 2007).

Aluminum is an element that has a conservative behavior. It is an elemental proxy for lithogenous input in a sediment. Because the concentration of aluminum is similar in acidic to basic extrusive, intrusive and most metamorphic rocks, it is used to estimate the total lithogenous content of a sediment, notably for determining aluminum concentration in bulk upper crust and shales. This situation is observed in the formation of soil and in weathering profiles because of the in situ formation of clay minerals and the retention of Al-hydroxides (Calvert and Pedersen, 2007). Thus, aluminum is used as a normalizing parameter in the study of sediments to assess relative enrichment or depletion degrees of

specific elements in a sample. It is also used for the estimation of the "background" contribution of elements derived from crustal sources (Calvert and Pedersen,, 2007).

A different method to normalize elemental data is the use of bulk Ti content of marine sediments. This analysis is used in situations where the total biogenous fraction of the deposits is small and all Al is contained in lithogenous aluminosilicate lattices. But Ti content varies to a greater extent in different rock types compared with Al (Calvert and Pedersen, 2007). This variation is why the use of Ti as a general lithogenous index is more complicated than that of Al. It is helpful to have a more or less uniform Ti content in a wide range of crustal reservoirs. Therefore, Ti/Al ratios have also been used as a grain-size proxy (Boyle, 1983).

Geochemical proxies are used to estimate redox conditions at both the sea floor and in below the sediment-water interface. Post-depositional precipitation or adsorption from bottom waters and from pore waters causes the accumulation of trace elements in the solid phase of marine sediments. The accumulation is controlled by redox reactions responding to a decomposition by oxidation of deposited organic matter (Froelich et al., 1979). The reactions leads to the consumption of the oxidants and accumulation of reduced species in the pore waters.

Different proxies are used for different oxygenation conditions of sedimentation: oxic, anoxic and suboxic conditions The proxies for oxic conditions of sedimentation include manganese, iodine and bromine. Manganese includes Mn(II), Mn(III) and Mn(IV) that are at valency states in Earth surface environments. Mn2+ and MnCl+ are the main soluble forms of manganese in seawater. This reflects the input of Mn as oxyhydroxide coatings on sediment particles and its partial release into solution. Mn(II) is thermodynamically unstable when there is oxygen and undergoes oxidation to insoluble Mn(III) and Mn(IV) oxides. At intermediate depths, a Mn maximum may occur in the

Oxygen Minimum Zone (where oxygen concentrations are below 100 mM). This shows reductive dissolution of settling particulate Mn oxyhydroxides or the lateral transport of dissolved Mn that has diffused out of anoxic shelf and slope sediments. Thus, manganese is an actively recycled element between oxidized and reduced forms across a redox boundary. Usually redox boundaries are within the sediment, but in some environments they can rise into the overlying water column, as is the case in the Black Sea and Saanich Inlet. The accumulation rates of terrestrial and biogenic detritus are slow compared to the precipitation rates of authigenic Mn under oxic conditions (Krishnaswami, 1976). Thus, enrichment of Mn exists in pelagic sediments (Goldberg and Arrhenius, 1958). Manganese is preserved in pelagic sediments due to the very low settling fluxes of organic matter. Therefore, anoxic deposits are characterized by Mn concentrations in solid-phase. They are completely controlled by the aluminosilicate fraction, and the surface sediments accumulate Mn oxyhydroxides. Manganese production, referred to as ‘‘manganese pumping,’’ occurs beneath oxygenated bottom waters only (Calvert and Pedersen, 2007). Anoxic basins have bottom sediments that are lacking authigenic Mn enrichments, which suggests that the “manganese pump” is only present under oxic bottom waters.

The halogens iodine and bromine are elemental proxies also used for the study of oxic conditions of sediments. The organic fraction of marine sediments and the diagenetic reactions involving organic matter degradation control the distribution and concentration of iodine and bromine in marine sediments (Bojanowski and Paslawska, 1970; Price et al., 1970). Iodine is depleted relative to bromine in anoxic environments (Price et al., 1970; Price and Calvert, 1977; Shimmield and Pedersen, 1990). Thus, enrichment of iodine relatively to organic carbon and bromine contents in marine sediments can be used as proxies for past oxygenated bottom water conditions (Calvert and Pedersen,, 2007).

Suboxic conditions exist where concentrations of oxygen are very low (ranging between 2 and 4 μM), at a level that is between oxic and anoxic. Enrichment of sediments with the elements Cr, V, Re, and U has been used as a proxy for sedimentation under suboxic conditions (Calvert and Pedersen,, 2007). These elements occur in seawater in at least two oxidation states, and they are removed to bottom sediments when there is a less soluble, lower oxidation state.

Chromium and vanadium are removed from pore waters of some continental margin sediments close to the depth of manganese oxide reduction. This means that they are diffusing into the sediments down a concentration gradient that is fixed at depth (Shaw et al., 1990). In pore waters of organic rich sediments, dissolved Cr and V concentrations increase with depth, as in the Gulf of California (Brumsack and Gieskes, 1983). This indicates that these elements become insoluble under low redox potential conditions.

In the organic-rich Miocene Monterey Formation, for example, enrichments of Cr and V are much larger than Mo and U enrichments, suggesting that sediment deposition occurred under suboxic conditions (Piper and Isaacs, 1995). Thus, Cr and V are present in deposits on an upwelling-intense continental margin (Isaacs, 2001).

Rhenium is characterized by higher enrichments in the suboxic sediments of near-shore and continental margin settings (Calvert and Pedersen,, 2007). Uranium has a constant concentration in all seawater oceanic basins (Ku et al., 1977), and is conservative in estuaries (Boroleet al., 1982; Cochran, 1984). In anoxic basins, U is removed from solution to the bottom sediments. Despite the fact that in this type of basin environment U is removed in the deep water, it exists in solution in its higher oxidation state. Thus, uranium removal from the sediments occurs by diffusion from the bottom water into the underlying deposits. Thus, we can predict changes in productivity by observing the changes in U in the bottom sediments. U is enriched in organic-rich sediments (Calvert and

Pedersen,, 2007). Bottom waters do not have to be completely under anoxic conditions for U enrichments to occur. There is also a relationship between the variations of the element U and TOC and an association between U, S and V. High values of U and S indicate the presence of high organic carbon, even if these relationships are clearly developed in some wells but not in others (Sano and Ratcliffe, 2013). This anomaly shows the complicated relationship between organic carbon content and geochemistry, which varies laterally across the Haynesville study area (Sano and Ratcliffe, 2013). Sulfur and TOC relationships can be disturbed in pyrite nodules and by pyritization of fossils. Changes in oxygenation, redox mineralization, and organic matter preservation are also governed by a chemical relationship.

Silver, cadmium, copper, nickel and zinc are chalcophile elements. They have a high affinity for sulfur, and their greatest concentration is found in the sulfide phase. They are commonly enriched in black shales. Higher concentrations of those elements are found in sulfide deposits in the Earth's crust. In the upper part of the oceanic water column, they are liberated from settling organic debris, and in surface waters they are removed quantitatively by plankton growth (Calvert and Pedersen,, 2007).

Cadmium is characterized by concentration-depth profiles that look very similar to the ones of the macro-nutrient phosphate during upwelling events (Calvert and Pedersen,, 2007). Thus, cadmium is considered to be a great upwelling proxy (Van Geen and Husby, 1996). Copper has a relatively unique profile and variation among the trace metals in seawater. It behaves partly like a micronutrient and at the same time, in deep water, it is scavenged from solution onto particle surfaces.

Some anoxic-basin case examples given by Calvert and Pedersen, (2007) and Algeo and Lyons (2006) are the Cariaco Trench, Framvaren Fjord, Saanich Inlet and the Black Sea. In those basins the dissolved concentrations of Cd, Cu and Zn decrease from the upper

oxic water mass into the underlying anoxic waters. In the bottom sediments of some modern anoxic basins, enrichment in Cd, Cu, Ni and Zn occur, but these enrichments are highly variable (Jacobs et al., 1987).

One of the main proxies used in anoxic basin studies is molybdenum (Mo). This element is removed from solution within the bottom sediments in anoxic basins (Calvert, 1990, 2007; Algeo and Manyard, 2004, 2009). Molybdenum enrichment in marine sediments happens in the presence of sulfide. Sulfide can increase in concentration to relatively high levels in subsurface continental margin sediments and in anoxic basins due to biological sulfate reduction. The largest sedimentary Mo enrichments are found in permanently anoxic basins, such as Saanich Inlet and the Cariaco Basin (Piper and Dean, 2002). Molybdenum is most likely fixed as Fe-Mo-S clusters, probably in solid solution in FeS phases (Helz et al., 2004). In anoxic sediments Mo can be hosted in pyrite (FeS2), which forms from FeS during diagenetic sulfide reactions (Huerta-Diaz and Morse, 1992).

The relationships between trace metal enrichment and TOC in shales are a great indicator of the factors controlling trace elements variations. Two behavioral patterns of trace metals that represent different responses to benthic redox conditions were identified. The first one involves a strong euxinic affinity, indicated by Mo, U, V, and Zn enrichment. The second behavioral pattern involves weak euxinic affinity, indicated by a low enrichment of Cu, Ni, Cr, and Co and a moderate to strong covariation with TOC displayed in samples with all levels of TOC (Algeo and Maynard, 2008). 2004).

One of the main trace elements-TOC relationships used is the ratio [Mo/TOC]s of the sediment that indicates [Mo]aqueous in water. A low [Mo]aq means that there is basin restriction, anoxic euxinic conditions and low renewal rates (Algeo and Maynard, 2004, 2009; Algeo and Rowe, 2012).

To confirm whether redox or hydrographic influences dominate in a given paleomarine system, a careful evaluation of trace-metal patterns in relation to redox proxies is required. Evaluation of the Degree of Pyritization (DOP) is an example (Algeo and Rowe, 2012). DOP is a measure of the ratio pyrite iron/(pyrite iron + reactive iron). A positive covariation between DOP and [Mo/TOC] indicates that there is redox control of trace-metal accumulation. This is the case in marine systems in which oxic or suboxic conditions prevail. On the other hand, if there is no related variation of DOP and [Mo/TOC]s, there is hydrographic control of trace-metal accumulation. This is the case in marine systems that are dominantly anoxic.

It is important to mention artifacts that might be encountered when using these proxies. These artifacts must be carefully evaluated and interpreted when making paleoceanographic analysis and deductions. Post-depositional migration or loss of authigenic metals are examples of the occurrence of these artifacts. If exposed to oxygen after initial accumulation, several authigenic trace metals can be remobilized and relocated in buried sediments. This post-depositional migration of authigenic metals allows the diffusion of dissolved oxygen into deeper anoxic sediments and will build up higher trace metals concentrations due to a higher burial flux of organic matter. Uranium can be lost from sediments due to bioturbation caused by the post-depositional transport of the reducing sediment to the near-surface. Molybdenum can be lost if anoxic sediments have been exposed to oxygen, unless it is associated with authigenic pyrite formation (Crusius and Thomson, 2000). Therefore, if the conditions are sufficiently anoxic for pyrite formation, Mo enrichments can be preserved in re-oxidized deposits. Authigenic metal records are well preserved in sediments that have high sedimentation rates and where the metal enrichments are permanently buried under suboxic or anoxic conditions. Because Ag, Cd, Cr, Cu, Mo, Ni, Re, U, V and Zn are all removed under suboxic and/or anoxic

bottom water conditions from seawater, it is important to distinguish well between these two environmental conditions of sedimentation. One method to distinguish between suboxic and anoxic environments involves the enrichment of Cr, Re, U or V accompanied by the absence of significant enrichments of Ag, Cd, Cu, Mo, Ni or Zn (Calvert, 2007). Another good way to make this distinction is by contrasting the geochemical behaviors of rhenium and molybdenum. Molybdenum is adsorbed on Mn oxyhydroxides and is also removed to anoxic sediments at high dissolved sulfide levels, which are maintained in the surficial sediment by anoxic bottom waters. Rhenium, in contrast, is strongly removed to suboxic sediments and not associated with authigenic oxide phases (Calvert, 2007). This is why if in a given sedimentary deposit, the total ratio of Re/Mo is greater than the ratio of seawater (0.4 mmol/mol), it is an indication of suboxic conditions. On the other hand, if the ratio is close to that of seawater, it is an indication of anoxic conditions.

Caution should also be used when evaluating trace-metal concentrations. Trace-metal/TOC relationships in hydrographic analyses can only be used on systems that had anoxic deep waters. The fact that the influence of redox variation on trace-metal accumulation patterns outweighs that of hydrographic factors in some paleomarine systems should also be taken into consideration (Algeo and Rowe, 2012).

Complementary to elemental studies, minerals and their variations are also very important proxies that indicate the sedimentary input and depositional settings in the basin. Aluminum oxide (Al_2O_3) variations are an indicator of clay input. Silicon dioxide (SiO_2) is also an indicator of clay content and input but also of detrital quartz and feldspars presence. Thus, the ratio (SiO_2/Al_2O_3) represents the ratio of quartz over clay. Calcium oxide (CaO) presence indicates calcite content in the basin. Sodium oxide (Na_2O) is a plagioclase indicator. Magnesium oxide (MgO) is an indicator of the amount of chlorite and amount of dolomite relationships; MgO concentration will follow the chlorite

distribution in the case of low dolomite, and it will follow the dolomite distribution in the case of dolomite abundance. Therefore, the ratio (Fe_2O_3/MgO) indicates the variation of pyrite: both these minerals are chlorite components, but pyrite does not contain MgO, and Fe_2O_3 is associated with pyrite, which makes this ratio helpful for the tracking of pyrite (Sano and Ratcliffe, 2013).

Major Element	Mineral Phase	Significance
Ca	Calcite Dolomite Phosphate Ferrous dolomite/Ankerite	Carbonate Deposition Diagenesis Phosphorus Preservation Diagenesis
Al, K	Clays (Illite, Kaolinite, Chlorite) Feldspars	Lithogenous input Diagenetic Signature
Si	Quartz Clay Feldspars	Can be Detrital or Biogenic Llithogenous input Diagenetic Signature
Fe	Pyrite Clays Ankerite	Anoxia/Euxinia Lithogenous input Diagenesis
Mn (Similar to Fe variation, except in pyrite)	Mn oxyhydroxides Mn carbonates	Oxic conditions
Mg (Follows Ca in Calcite)	Calcite Dolomite Ankerite	Carbonate Deposition Diagenesis
Ti (Similar to Ga, Th, Nb, Zr)	TiO_2 $FeTiO_3$ Clay	Detrital (No Biologic Signature) Lithogenous input
P	Phosphate Minerals (e.g. Apatite) Franklinite Collophane	Can be organic or inorganic (Biological Detritus e.g. Fish Bones) Organic-Inorganic Bound
S	Sulfide Organic Matter	Anoxia

Table 1: Major elements and their significance in a depositional environment context.

Trace Elements	Mineral Phases	Significance
Ni (similar to silicic acid)	Organic presence signature Sulfide deposits Clays	Liberated from settling organic debris in the upper part of the water column Removed quantitatively by plankton growth in surface waters
V	Organics Clays	Detrital input
Mo	Organics Sulfides Clays (1-3 ppm) Fixed in Fe-Mo-S clusters (in solid solution in FeS phases) Hosted in pyrite (FeS_2) Organic matter	Removed from the anoxic waters within the bottom sediments
U	Organics Phosphates	Paleoproductivity Redox
Y	Phosphates Phosphate minerals structures Clay	Productivity on Phosphate preservation
Th	Clay	Detrital input
Cu (similar to micronutrients)	Organic presence signature Primary productivity indicator Sulfide deposits	Liberated from settling organic debris in the upper part of the water column Removed quantitatively by plankton growth in surface waters
Zn (similar to silicic acid)	Organic presence signature Primary productivity indicator Sulfide deposits	Liberated from settling organic debris in the upper part of the water column Removed quantitatively by plankton growth in surface waters

Table 2: Trace elements and their significance in a depositional environment context.

Ag (similar to silicic acid)	Organic presence signature Sulfide deposits	Liberated from settling organic debris in the upper part of the water column Removed quantitatively by plankton growth in surface waters
Cd (like phosphate during upwelling events)	Organic presence signature Sulfide deposits	Upwelling proxy Liberated from settling organic debris in the upper part of the water column Removed quantitatively by plankton growth in surface waters

Table 2 continued: Trace elements and their significance in a depositional environment context.

Chapter 2: Methods

A chemostratigraphic analysis was conducted on the T. W. George core, from Harrison County, East Texas, using X-ray fluorescence (XRF) and X-ray diffraction (XRD). In addition, a hardness test was performed on different samples along the core using the Equotip Bambino 2. A core description and a Hierarchal Cluster Analysis complemented the chemostratigraphic studies.

1. XRF

For XRF analysis, the Bruker S1 Tracer III-V hand-held energy dispersive tool was used as the main instrument for the analysis (Rowe et al., 2012). Every sample was placed on the flat horizontal tray on top of the stationary instrument, where X-rays penetrate the core through an oval window of dimensions 3 x 4 mm. Samples were taken every 2 inches, and both major and trace elements were measured separately for the same core sample. For the measurement of major elements, the instrument was set for 15kV, and every sample was scanned for a period of 30 seconds, using a vacuum pump linked to the XRF instrument. The instrument? The vacuum? maintains a pressure of less than 3 Torr to remove the air between the window and the detector. For trace-element measurements, the instrument was set to 40 kV, every sample was scanned for 90 seconds, no pump was used, and before starting the scanning process, a Ti-Al element filter was inserted into the XRF.

The XRF works as follows. When the instrument is receiving electric power, the x-ray tube is activated dispersing x-rays on the core sample being analyzed by the instrument. These x-rays strike the inner shell electron of the atoms in the sample, ejecting this electron from the atom. The X-ray energy has to be higher than the absorption edge of the element, the adsorption edge being the lowest energy at which a vacancy can be created in the shell. This displacement will create a vacancy in the inner shell. Another electron will move from

an outer shell to fill the vacancy. This causes an X-ray photon to be released and hit the analyzer's SiPIN detector. Every element releases unique photon energy, which allows the detection and quantitative analysis of the specific elements in every sample.

The instrument is connected to a computer controlling all data acquisition, and a qualitative real-time spectrum is displayed for every sample (Figure 5). After data acquisition, elemental calibration is set for every element measured by the XRF instrument (Rowe et al., 2012). It should be noted that U is usually not well calibrated for XRF.

Figure 5: Set-up of Bruker XRF Tracer- SD used for X-ray fluorescence elemental data collection.

2. BAMBINO HARDNESS

Hardness tests were performed in order to find a correlation between elemental composition and the core hardness variations. The Equotip Bambino 2 was used, which is a hand- held portable instrument that uses non-destructive impact from its testing nozzle at its tip. This instrument is mostly used for metal-hardness measurements. It measures

hardness using the Leeb rebound method developed by Proceq SA. It registers results, displays readings and allows real-time monitoring of hardness data using Piccolink software (Zahm and Enderlin, 2010).

The main principle of the method is based on calculating a hardness value by comparing the energy of a body before and after impacting a sample (in this case, the core sample). This energy quotient is calculated from comparing the impact and rebound velocities of the impact body (Zahm and Enderlin, 2010). The rebound from harder samples is faster than the one from softer ones. Prior to testing the core samples, 3 to 10 test impacts were performed on a reference hardness object to ensure that the device was operating correctly. When used on the T.W. George core, this method generated inconsistent hardness data with large gaps between values. Thus data generated by the Equotip Bambino 2 was not included in the results or discussion of this thesis.

Core Analysis	Number of Samples	Interval	Analysis Specifics	Instrument	Instrument settings
XRF Analysis	2084	Every 2 inches	Hand-held elemental X-Ray Fluorescence of major and trace elements on slabbed core	Bruker Tracer-SD	Majors: 15 kV, 30 µA Vacuum, No Filter Traces: 40 kV, 11.9 µA, No Vacuum, Ti-Al Filter
XRD Analysis	53	1-2 per box	Powdered samples drilled from the back of the core, run on X-ray diffraction using 15 mg for analysis	Olympus in-situ BTX	5-55˚ 2Θ 30 kV 10 W
TOC	301	1 foot	Powdered samples drilled from the back of the core, using 15-20 mg for analysis	Costech ECS 4010	ECS 4010 coupled via conflo- III to Thermofinnigan Delta-V
Bambino Data	300	1 foot	Hand- held instrument placed perpendicular to the core sample. Performing 5 to 7 impact hits on each sample	Equotip Bambino 2	Testing method: Leeb rebound Impact energy: 11.5 Nmm (impact body Equotip D) Spherical test tip: Tungsten carbide, 3 mm diameter

Table 3: T. W. George core study analysis.

3. HIERARCHAL CLUSTER ANALYSIS

Hierarchical Clustering is a statistical data analysis tool that seeks to build a hierarchy of clusters, based on sample similarities. In this thesis, the samples with the most chemical similarities are put into one cluster. The XRF data of the T.W. George core were

used. The samples are divided between 15 different clusters and displayed on a dendogram and on a “heat map” (Figure 15) using Spotfire software.

Chapter 3: Results

1. Core Description

Figure 6 presents the different macro-facies observed in the T. W. George core. Figure 7 is a stratigraphic column presenting the different facies shown in the T. W. George core and their lithologies and characteristics. This information is used to complement the chemostratigraphic results to provide a more complete understanding of the sequence stratigraphy of the Haynesville Formation.

Three main facies were identified by naked eye after a core description of the Haynesville:

- Homogeneous mudrock
- Laminated mudrock
- Bioturbated mudrock

Pyrite fills were present at the bottom of the core. Calcite-filled fractures were observed at the bottom and in the middle of the core.

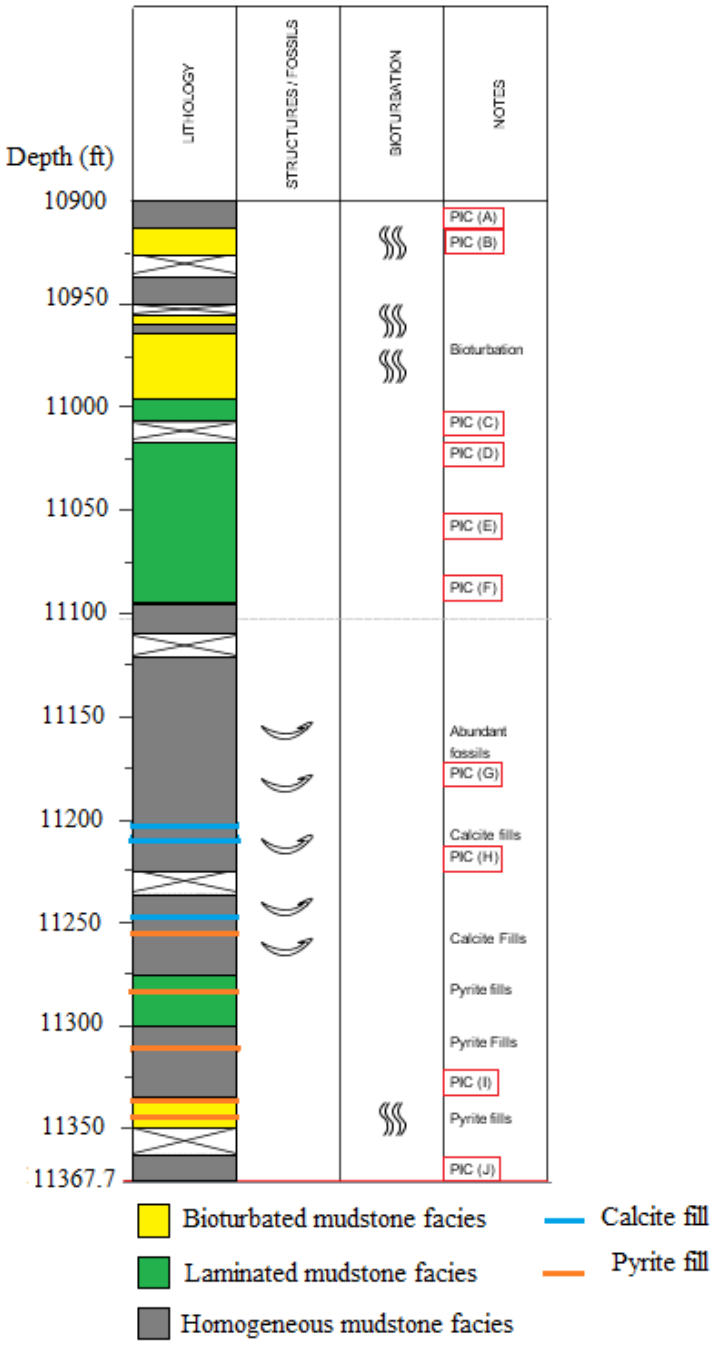

Figure 6: Stratigraphic column of the T. W. George core based on core description on a macroscopic scale. Core pictures depths in Figure 14 are indicated by red squares

A) Massive black homogeneous mudstone facies. Depth: 10,902 ft.

B) Bioturbated mudstone facies with minor presence of shell fragments, some overturned by bioturbation. Depth: 10,907 ft.

C) Laminated mudstone facies. Mudstone (dark) and claystone (light) alternations. Presence of micro-calcite fractures. Depth: 10,992 ft.

D) Laminated mudstone facies with boudinage shaped laminations. Depth: 11,029 ft.

Figure 7: High resolution core scans from the T. W. George core. Note: Images have been modified for contrast. Core depth can be found on Figure 17.

I) Homogeneous mudstone facies with parallel-to-bedding-plane calcite-filled fractures. Depth: 11,229 ft.

J) Mudstone with parallel-to-bedding-plane discontinuous pyrite-filled fractures. Depth: 11,286 ft.

K) Mudstone with parallel-to-bedding-plane discontinuous pyrite-filled fractures. Depth: 11,307 ft.

L) Fissile facies showing fine parallel-to-bedding-plane calcite-filled fractures. Depth: 11,363 ft.

Figure 7 continued: High resolution core scans from the T. W. George core. Note: Images have been modified for contrast. Core depth can be found on Figure 17.

E) Laminated mudstone facies with some discontinuous plane laminations. Presence of micro-calcite fractures. Depth: 11,073 ft.

F) Laminated mudstone facies with sharp contact surface between laminations. Depth: 11,093 ft.

G) Homogeneous mudstone facies with scattered bivalve shell fragments shown as white fragments in the core. Depth: 11,175 ft.

H) Homogeneous mudstone facies with scattered bivalve shell fragments shown as white fragments in the core. Depth: 11,176 ft.

Figure 7 continued: High resolution core scans from the T. W. George core. Note: Images have been modified for contrast. Core depth can be found on Figure 17.

2. XRD MINERALOGY

The XRD data presented in Figure 8 (a) show the mineralogy variations of pyrite, dolomite, albite, quartz, kaolinite, illite and calcite with depth. From the bottom of the core (11,370 ft) to depth 11,300 ft, an equal distribution in the mineral phases is recorded in which no particular mineral dominates. Between 11,300 ft and 11,230 ft, calcite percentage increases in the core. Illite and kaolinite decrease slightly in percentage, and quartz is relatively constant. Albite, dolomite and pyrite are relatively constant. From depth 11,230 ft to 11,150 ft, the amount of calcite increases relative to the underlying package. The amount of illite, kaolinite and quartz decreases. The percentage of albite, dolomite and pyrite is relatively stable. Between 11,150 ft. and 11,115 ft., the highest increase in calcite values is observed, reaching values between 65% and 70% in the samples. Illite, kaolinite, quartz concentrations decrease in the core, reaching their lowest values. Albite, dolomite and pyrite are generally unchanged. Between 11,115 ft and 11,105 ft, the lowest calcite percentage is observed, as is the highest dolomite percentage, with a peak of 70 %. Illite, kaolinite, quartz and albite have very low percentages at those depths. Pyrite content remains relatively the same. Between 11,105 ft. and the top of the core, the concentrations of illite, kaolinite and quartz increase, reaching their highest in the shallowest depths. Calcite concentrations decrease in these samples with a mineral percentage ranging between 20% and 30%. Albite, dolomite and pyrite have the same percentages as those in the bottom part of the core.

3. TOTAL ORGANIC CARBON

Total organic carbon (TOC) data (Mainali, 2011) are displayed in Figure 8 (b), which shows TOC variation with depth. In terms of TOC content, the T. W. George core is clearly divided into two parts. The deeper one, from depths of 11,370 ft. to 11,100 ft., displays high TOC content between 2% and 4%. The overlying part, from 11,100 ft. to

10,900 ft, displays a lower TOC content of less than 1%. There is a small transitional phase between these two parts of the core, from depths 11,110 ft to 11,060 ft with TOC content of between 1% and 2%. The first TOC-rich ore section represents the Haynesville Formation and the overlying TOC-poor section represents the Bossier Formation, with a transitional phase between them.

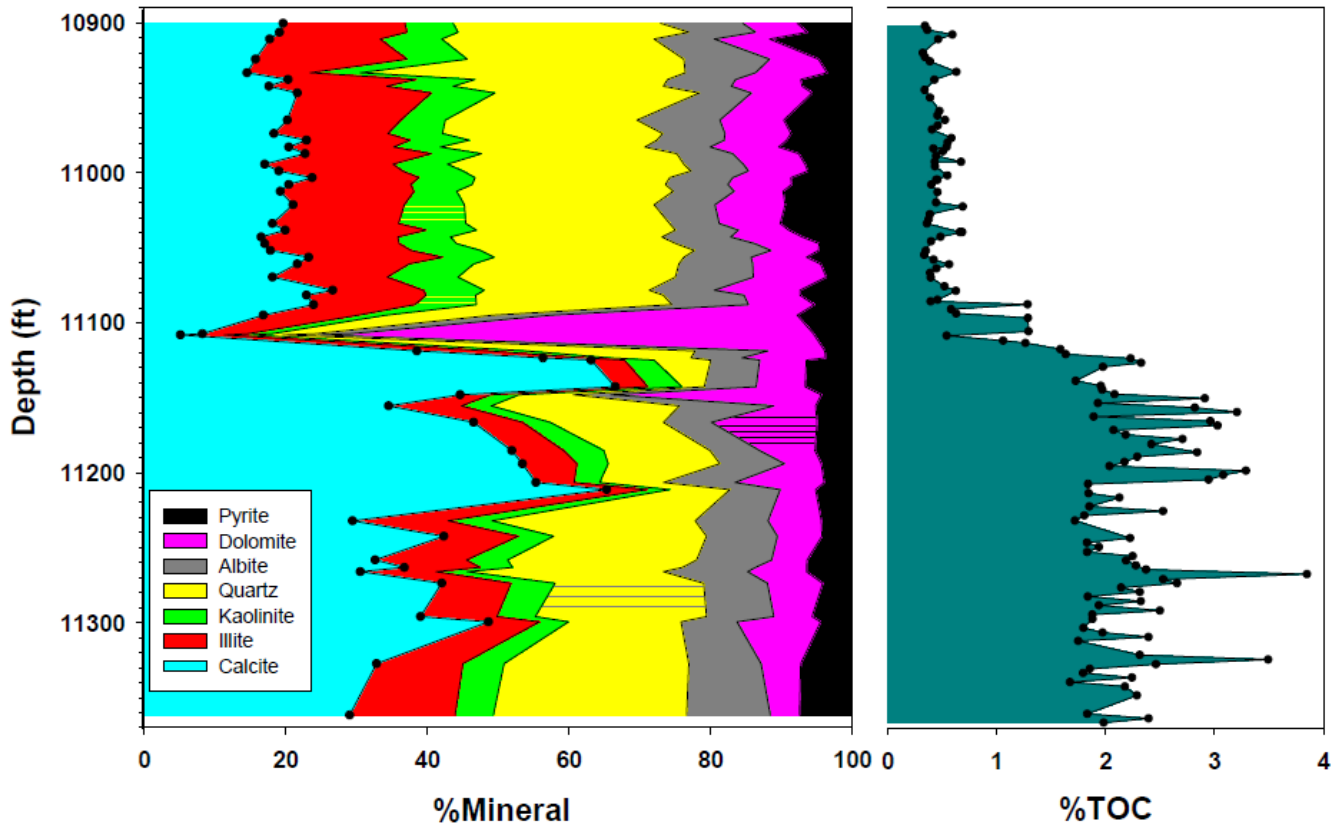

Figure 8: (a) Mineralogic variation (b) TOC variation.

4. XRF CROSS-PLOTS: DETRITAL HOSTED ELEMENTS

The XRF data presented in Figure 9 show detrital elements such as Si, Ti and K (in percentage) vs. %Al, as well as %Ca vs. %Al and the two trace elements Ga and Th (in ppm) vs. %Al. These are major and trace elements are normalized to clay content because Al is a proxy for clay input. Si, Ti, K, Ga, and Th show a linear trend with a positive slope when plotted versus Al. A sample with high %Al has a high %Si, %Ti, %K, Ga (ppm) and Th (ppm) content. Some samples with a relatively high %Al (~8 %) show a very low %Ca (between 0 and 2% content). For the samples that show a trending variation between %Al and %Ca, this trend is linear and characterized by a negative slope. The plot displaying %Ca versus %Al shows that samples with high %Al have low %Ca and vice versa. Figure 10 represents the cross-plot of iron vs. aluminum. The data are distributed between two main populations, one displaying a linear trend between the two elements in the core, the other showing data points occurring above the Fe-Al line.

When generating XRF measurements, the core sample at depth 10,999.083 ft showed a high Ga content of 44 ppm that is above the Ga curve. Given that the average Ga content of the core is 18 ppm, this measurement is abnormally high. After further investigations, the high Ga content measurement appears to be influenced by a high amount of Zn in this particular sample.

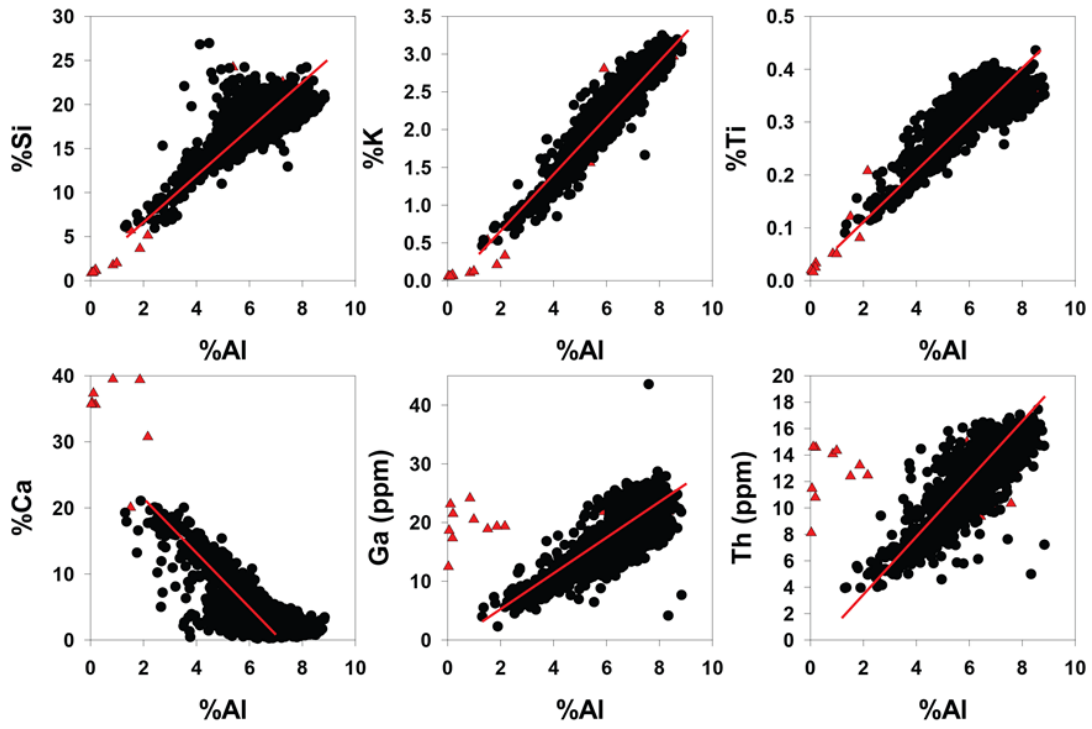

Figure 9: Cross-plots of percentages of detrital elements including %Si, %Ti and %K vs. %Al, as well as %Ca (representing calcite) vs. %Al and the two detrital trace elements Ga and Th (in ppm) vs. %Al.

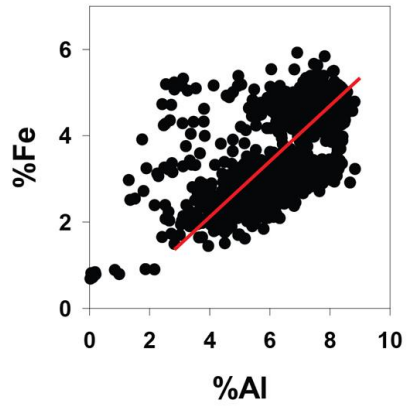

Figure 10: Cross-plot of iron vs. aluminum.

5. XRF Cross-Plots: Carbonate Hosted Elements

In Figure 11, the elemental content %Mg, %Fe, %Mn, %K and %Si vs. %Ca, and the Sr content in ppm vs. %Ca, are displayed. These cross-plots allow the identification of elements present in the calcareous phase. The data are distributed between two main populations, one displaying a trend between the two elements, the other showing data points with very low %Ca (%0 to %2); this population of samples can be identified on all cross-plots. The plot of %K vs. %Ca shows a negative trend. When Ca increases in a sample, K decreases. The plot of %Si vs. %Ca also shows a negative trend. As Ca increases, Si decreases. The plot of %Fe vs. %Ca does not show any defined linear trend between the samples. Similar variations are also observed in the plots of %Mg vs. %Ca and %Mn vs. %Ca that display no defined linear trend. Finally, in the plot of Sr (ppm) vs. %Ca, Sr covaries with Ca.

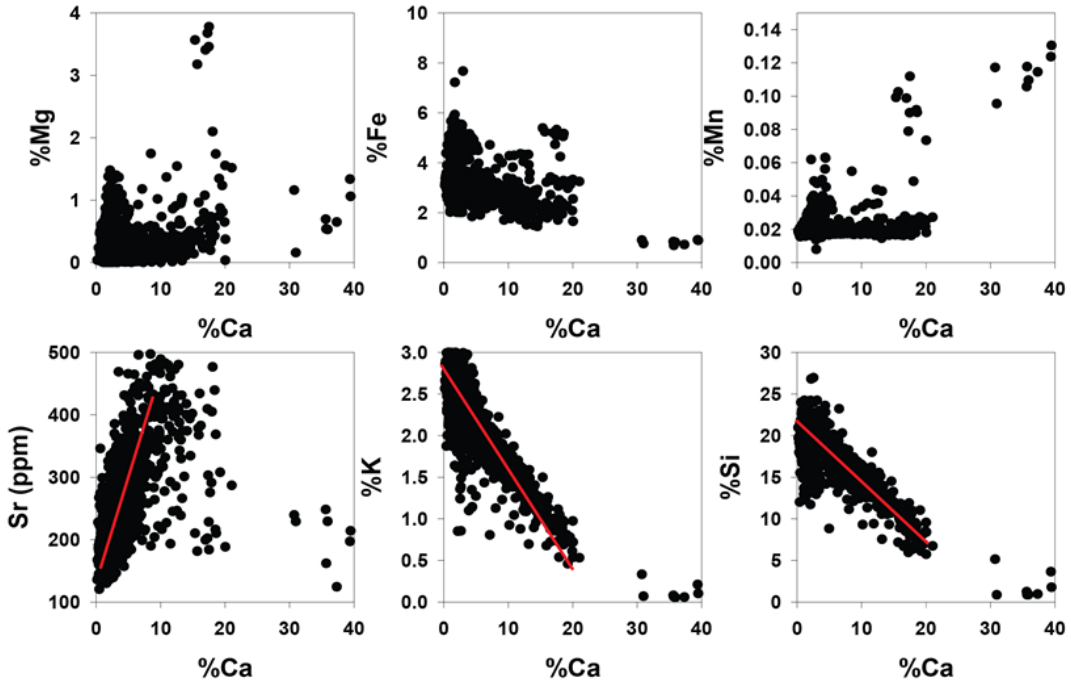

Figure 11: Cross-plots of elemental content %Mg, %Fe, %Mn, and Sr (ppm) (carbonate elements) vs. Ca, as well as %K and %Si (detrital elements) vs. %Ca.

6. CHEMOSTRATIGRAPHIC VARIATIONS OF ELEMENTS WITH DEPTH

In Figure 12 the chemostratigraphic variations of the major elements Al, Ca, Fe, and Mn (in percentage) and the normalization of Si/Al with depth are displayed

Aluminum variation with depth: Al concentrations are higher at the top of the core. High Al values are observed at the bottom of the core between the depths of 11,367 ft and 11,320 ft. Average value is 6.7 %. Aluminum values decrease at around depth 11,320 ft to depth 11,063 ft, with values averaging 5.8 %. Around depth 11,063 ft up to the top of the core, Al values increase again, with an average value of 7.2 %.

Ca variation with depth: Low Ca values are observed at the bottom of the core between the depths 11,367 ft and 11,320 ft,with an average content of 3.5%. Ca values increase in the depth interval between 11,320 ft. and 11063 ft, with an average content of

4.8%. Around 11,063 ft. up to the top of the core, Ca values decrease again and are the lowest recorded, with an average content of 2.6%.

Fe variation with depth: Fe content is higher in the top part of the core. Between the depths 11,367 ft. and 11320 ft.\, Fe values have an average of 3.1%. In the depth interval 11,320 ft to 11063 ft, a slight decrease in Fe content occurs, with an average of 2.9%. Around 11,063 ft. up to the top of the core is a clear increase in Fe content, the highest recorded in the core, having an average of 4.6%.

Mn variation with depth: Mn concentrations are more elevated at the top of the core. Between the bottom of the core and 11,320 ft, Mn values are the lowest, with an average value of 0.02%. At 11,320 ft a slight increase in Mn content is observed, up to depth 11,063 ft. Around 11,063 ft up to the top of the core, a further increase in Mn content is observed, reaching its highest values recorded in the core, with an average of 0.03%.

Si/Al variation with depth: The Si/Al ratio is higher at the bottom to middle part of the core. We observe low Si/Al values between the bottom of the core and 11,320 ft. The Si/Al ratio increases at around 11,320 ft until 11,063 ft. At 11,063 ft to the top of the core, the Si/Al ratio decreases again.

It should be noted that the few outliers (8 samples) present in a small depth interval between 10,930 ft. and 10,936 ft., show abnormal recording of elements concentrations. This is applicable to these 8 samples when plotted for any element. They show extremely low %Al (as low as 0.04%) and %Fe (as low as 0.7%), and very high values of %Ca (around 40%) and %Mn (as high as 0.14%).

Figure 13 also shows chemostratigraphic variations of the trace elements Mo, V, Ni, Zn and As in ppm with depth.

Mo variation with depth: We clearly observe a high Mo content at the bottom of the core. Between depths 11,367 ft and 11,320 ft, a high Mo content exists, with an average

content of 23 ppm and values reaching up to 59 ppm. Between depths 11,320 ft and 11,090 ft, we observe a lower Mo content with an average content of 5ppm. Around 11090 ft to the top of the core, there is even more decrease in Mo content with an average content of 1 ppm and a many samples dropping to 0 ppm (some samples recorded negative Mo values).

V variation with depth: We observe a high V content at the bottom of the core. At the bottom of the core, between depths 11,367 ft and 11320 ft, we see a high V content with an average of 42 ppm and reaching 107 ppm. From depth 11,320 ft and up we see irregular variations with relatively low V content and an average of 4 ppm. At 11,063 ft up to the top of the core, we see a relative increase in V content with irregular fluctuations ranging from values as low as 0 ppm to values as high as 107 ppm, with an average content of 15 ppm.

Ni variation with depth: We observe the highest Ni values at the bottom of the core between the depths 11,367 ft and 11,320 ft with values with an average value of 76 ppm reaching up to 99 ppm. We see a clear decrease in Ni content at around 11,320 ft until the depth of 11,063 ft with Ni values averaging 50 ppm. Then Ni increases again at around 11,063 ft up to the top of the core with an average value of 62 ppm.

Zn variation with depth: Zn is significantly higher at the top of the core. Between the bottom of the core and depth and 11,320 ft, we have a Zn average content of 34 ppm. We observe low Zn values from 11,320 ft to 11,063 ft, as low as 0 ppm with occasional increases (e.g., at 11,197 ft, Zn content is 370 ppm) and an average value of 5 ppm (some samples show a negative value of Zn). Then we observe an increase in Zn content, reaching its highest values starting around 11,063 ft up to the top of the core, with an average content of 68 ppm.

As variation with depth: As variation in the core is not as definite and clear as Zn variation, but we can distinguish the following. We observe a high As package at the bottom of the core between the depths 11,367 ft and 11,320 ft, with an average value of 11 ppm. We see decrease in As content from the depths 11,320 ft to 11,063 ft with As values highly fluctuating between 0 ppm and 15 ppm, and an average value of 7 ppm. (Some As values are too low to be measured.) At around 11,063 ft, As increases again until the top of the core, with values averaging 10 ppm.

Figure 14 displays the variations of detrital elements with depth and of the element sulfur with depth. We observe peaks of Si in the depth interval 11,110 ft and 11,120 ft, as well as in the depth interval 11,220 ft and 11,240 ft. At these same depth intervals, we observe elevated amounts of Ti and Zr. The elements Si, Ti and Zr are co-varying across the core. We see a high sulfur content in the bottom part of the core compared to the overlying parts of the core that have a lower sulfur content.

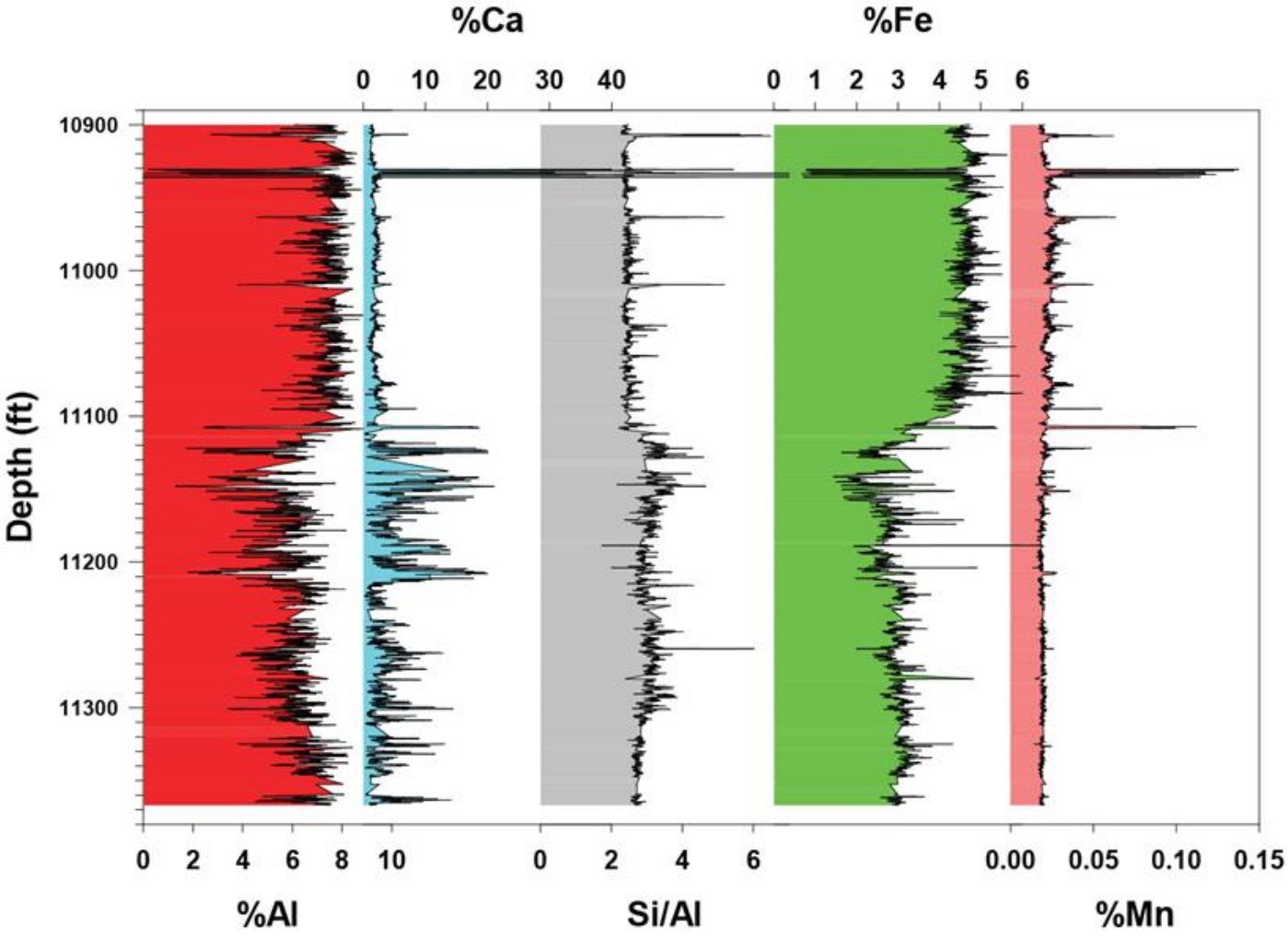

Figure 12: Chemostratigraphy of major elements and Si/Al ratio

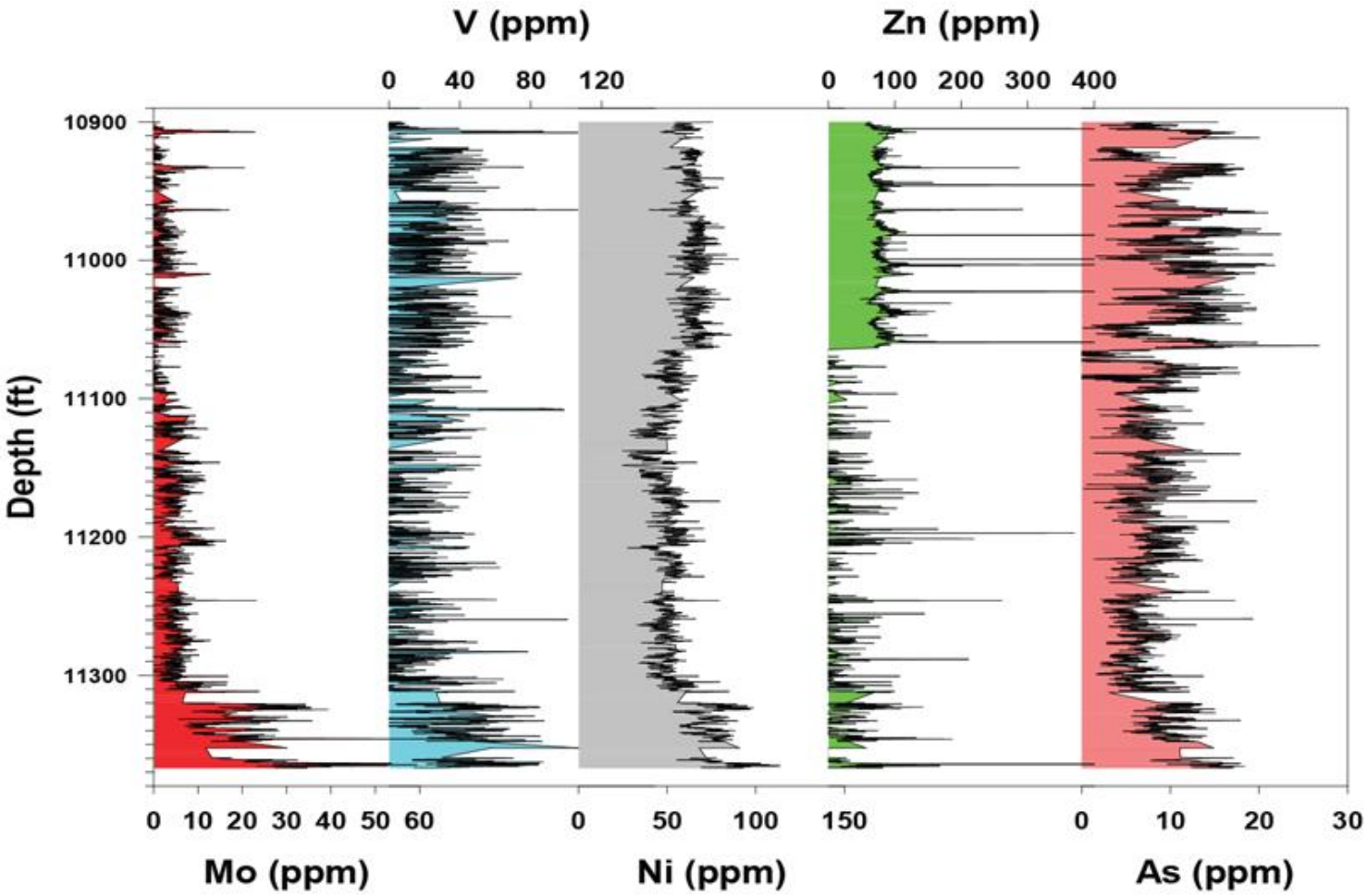

Figure 13: Chemostratigraphy of trace elements

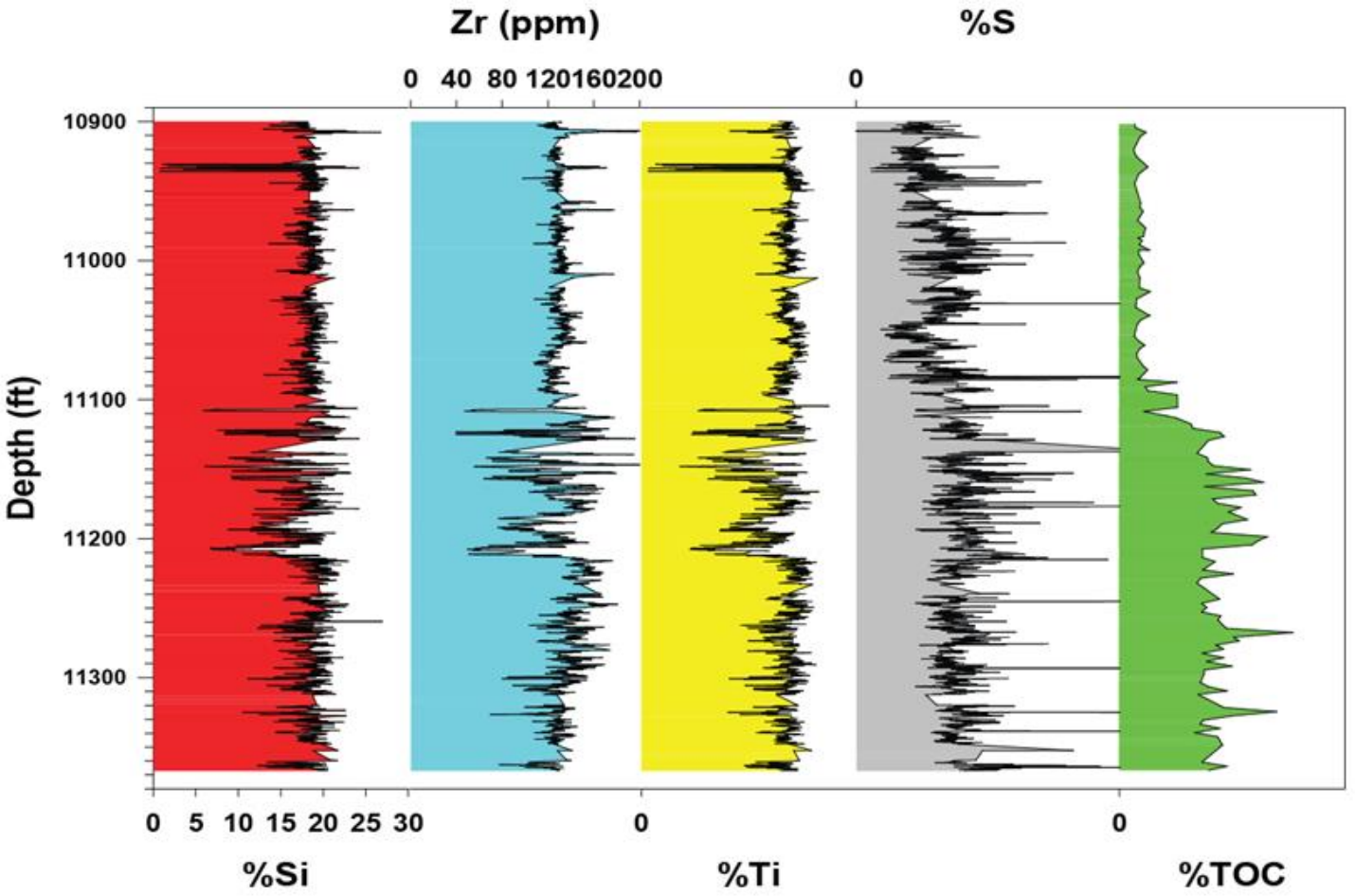

Figure 14: Chemostratigraphy of detrital elements and sulfur

7. CA-SI-AL TERNERY DIAGRAM

The Ca-Al-Si ternary diagram in Figure 15 allows comparison of the major components presence in the formation: clay, silica and carbonate and their variation in the core. The diagram uses normalized weight percentages of calcium oxide (CaO), aluminum oxide (Al2O3), and silicon dioxide (SiO2): SiO2, 5 X Al2O3 and 2 X CaO (Brumsack, 1989). The Haynesville Formation is dominated by carbonates. Al represents clay content, Si represents quartz content and Ca represents carbonate content. Observing the samples along the calcite dilution line, it is notable that the decrease in clay particles has a direct relationship to the increase in carbonate. The more calcite increases, the more quartz and clay are diluted.

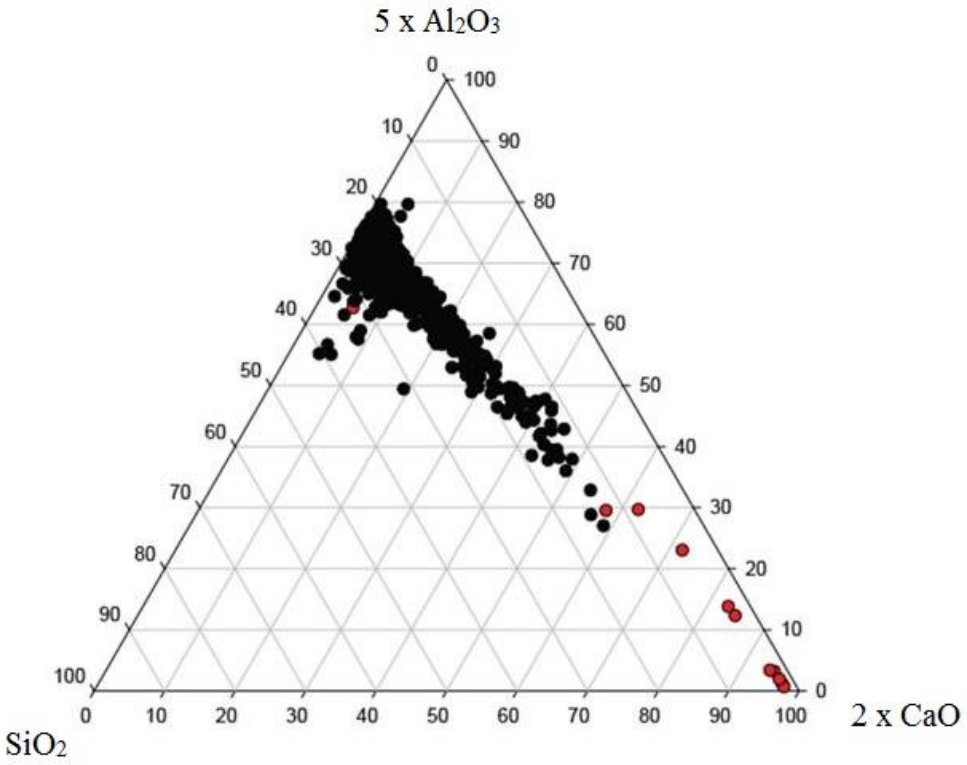

Figure 15: Ternary diagram representing the Ca-Al-Si relationship of the T. W. George core from the East Texas Basin (Brumsack, 1989). Red data points are out-of-range values.

8. BULK ELEMENTAL MINERALOGY TRENDS

Figure 16 shows the bulk elemental mineralogy trends. This is the elemental percentage of aluminum, potassium in the clay mineral phase, the percentage of calcium in the calcite mineral phase and the percentage of silica in the quartz mineral phase. The plot %Al vs. %Clay behaves in a linear trend with a positive slope. A similar behavior is displayed in the plot %K vs. %Clay, where a linear trend with a positive slope is displayed in the samples. Aluminum and potassium are dominant elements in the clay mineral phase. This complements the %Al results obtained by the data in Figure 12. As for the plot %Ca

vs. %Calcite, there is no definite linear trend. Samples are scattered across the plot, but the %Ca is clearly proportional to calcite content. Low %Ca values of between %1 and %5 are observed with a low calcite mineral percentage, and high %Ca up to %20 is observed with a high calcite mineral phase percentage of %45. Thus, calcium is the dominant element in the calcite mineral phase. The %Si/Al plot shows values between %2 and %4 in the quartz mineral phase.

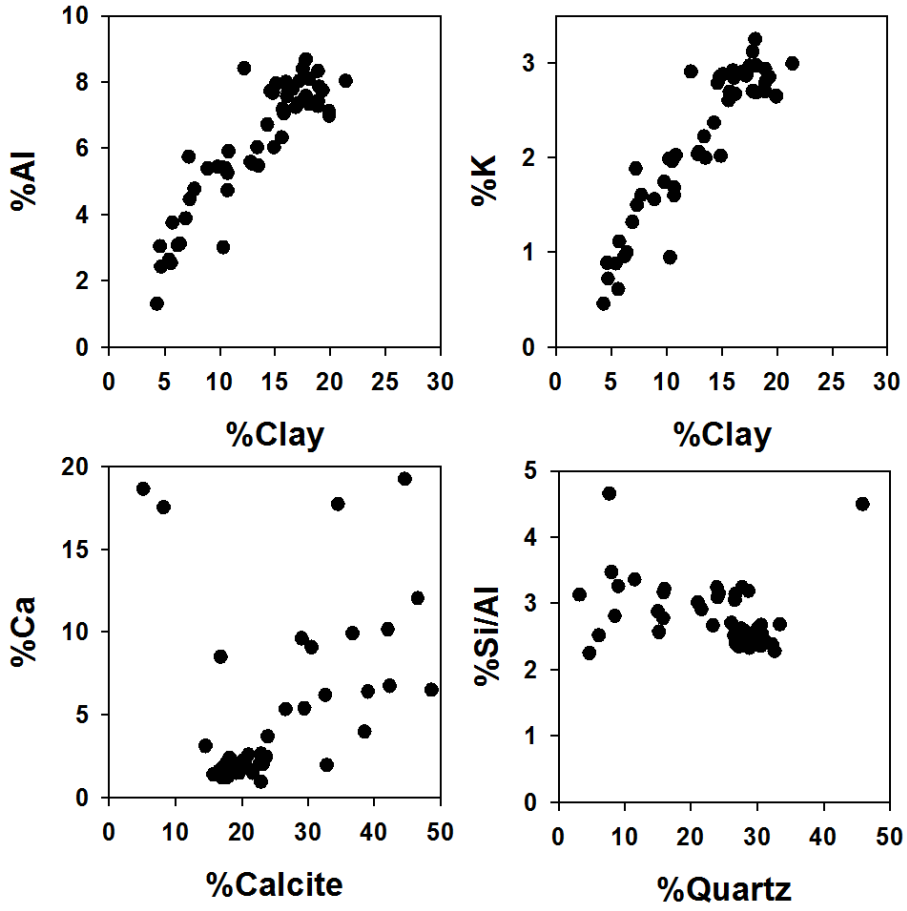

Figure 16: Bulk Elemental-Mineralogy Trends

9. ELEMENTAL PROXIES OF TOC

Figure 17 shows the elemental proxies of total organic carbon (TOC). It reveals the variation of the trace elements molybdenum, nickel, vanadium and uranium with total organic carbon.

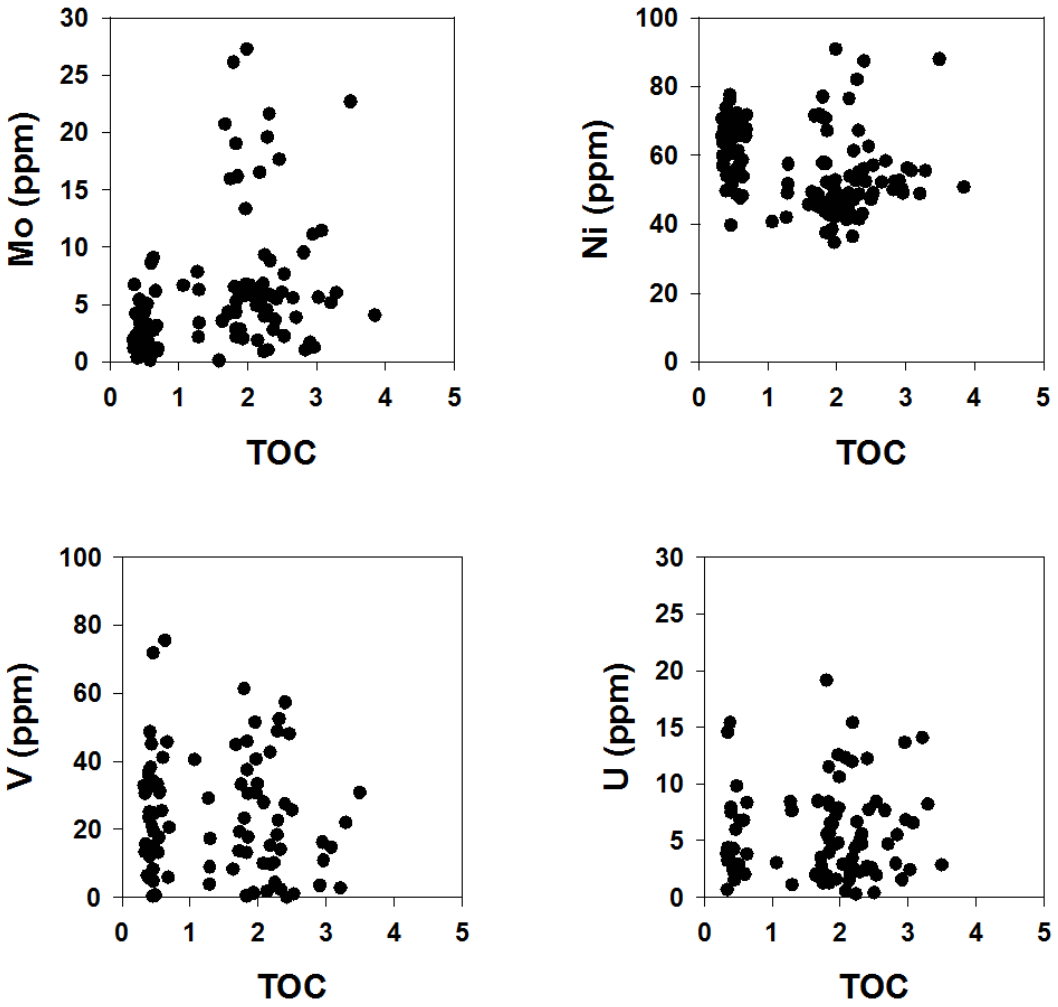

Figure 17: Elemental proxies of TOC

10. HIERARCHAL CLUSTER ANALYSIS

Figure 18 displays the HCA heat map generated by the Spotfire software, showing chemical distribution of the 15 different clusters. The order of the chemical elements on the heat map was selected based on elements similarities. The order chosen was the following: Ca, Sr, Mn, Mg (Carbonates); Si, Al, Ti, Th, Ga, K, Rb, Zr, Cr, Nb (Detritals); S, Fe, As, Co, Pb (Chalcophiles); Ni, Cu, Zn (Chalcophiles and organo-philes); V, Mo, U (Redox indicators); P, Y (Phosphates).

Figure 19 displays the cluster stratigraphy graph showing the distribution of the 15 clusters along the depth of the core. Table 4 (a) and Table 4 (b) show the 26 chemical elements' distribution in the 15 different clusters by order of enrichment. The cells of main elements are colored in Table 4 (a) and Table 4 (b). These colors help in visually tracking the different elements in each cluster and in comparing their occurrence in other clusters. The following elements were assigned the following colors:

- Zn, Cu and Ni: orange
- Mo and V: dark gray
- Mg: purple
- S and Fe: pink
- Si: yellow
- P: green
- Al: light gray
- Ca: blue

Table 5 displays the characteristics of each clusters according to the chemical elements' distribution. The chemical elements allow the characterization of the chemical facies and their labelling: When the elements S and Fe are both enriched, it indicates the presence of pyrite. On the other hand, when they are not simultaneously enriched, it might

indicate the presence of an ash bed due to volcanic activity. When Zn and Cu are high and proximal to each other in composition, this may indicate the possibility of primary productivity. P is also an indicator of primary production and is present in fish bones, thus possibly indicating the presence of a bed of fish bones. It can also be an indication of slow sedimentation. An enrichment in Mg and Ca indicates the presence of the dolomite mineral whose chemical formula contains the two elements. The proximity of Ca to the elements P and V is an indication of the presence of biogenic calcite. An enrichment in both Mo and V indicates a highly restricted depositional environment leading to organic matter preservation and dominated by anoxic or euxinic conditions. On the other hand, when V and Mo are very low, they indicate a more oxygenated environment.

Thus, the following labels were assigned to each of the 15 clusters:

- Cluster 1: This chemical facies has high Mg (4.98) and high Ca (4.87). An enrichment in both Mg and Ca indicates the presence of dolomite, whose chemical formula contains the two elements: CaMg(CO3)2. Thus it is classified as a dolomite. It also has a relatively elevated amount of V (2.67) and Fe (0.86) has a relatively average value, which is why it can be considered as suboxic. Cluster 1 is labeled as “Suboxic Dolomite.”
- Cluster 2: This chemical facies is highly enriched in Mg (2.54). It has detrital elements dominating, such as Al (1.14) and K (1.14). Si displays arelatively average value (1.03). Thus, it is classified as detrital. Because an enrichment of U (2.00) and Co (1.34) is observed, the cluster is considered to be U-suboxic. Cluster 2 is labeled as “U-Suboxic Detrital.”
- Cluster 3: This chemical facies has detrital elements dominating like Al (1.13) and K (1.13). Thus it is classified as detrital. It is highly enriched in Zn (2.68) and Cu (2.64), both indicators of primary productivity. With a high V (1.78) and Mg (1.77)

but low Mo (0.35), it is considered High-V suboxic. Cluster 3 is labeled as "High-V Suboxic Detrital."

- Cluster 4: This chemical facies is enriched in P (1.35). It does not display any high enrichment, but it has an average Ca (1.21). Cluster 4 is labeled as a "phosphate."
- Cluster 5: This chemical facies is enriched in P (2.09) and has also a relatively high S (1.47). Cluster 5 is labeled as a "phosphate, slightly sulfidic."
- Cluster 6: This chemical facies is enriched in Al (1.11) and has a relatively average Ca (0.86). Thus, it is classified as marl. Because an enrichment in V (1.58) and Co (1.98) with an average Fe (1.20) is observed, the cluster is considered V-Co-suboxic. Cluster 6 is labeled as a "V-Co-Suboxic Marl."
- Cluster 7: This chemical facies has average Al (1.02) and Ca (0.83), thus it is considered a marl. Because enrichment in Mo (3.87) and V (3.51) with a high value of U (2.80) is observed, the cluster is classified as euxinic. Cluster 7 is labeled as "Euxinic Marl."
- Cluster 8: This chemical facies has average Al (0.95) and Ca (0.72), thus it is considered a marl. Because of enrichment in U (2.52) with relatively high Mo (1.13) and s very low Zn (0.07) and Cu (0.06) is observed, the cluster is considered as anoxic. Cluster 8 is labeled as "Anoxic Marl."
- Cluster 9: This chemical facies is highly enriched in Ca (2.17) with a low Al (0.80), thus it is considered a limestone. It is also highly enriched in P (3.69) which makes it phosphatic. Cluster 9 is labeled as "Phosphatic Limestone."
- Cluster 10: This chemical facies is enriched in Al (1.15) and low in Ca (0.47); thus, it is considered detrital. Because high Cu (2.47) and Zn (1.97), indicators of primary productivity, are observed with Mg (1.91) and very low V (0.43), the cluster is classified as low-V suboxic. Cluster 10 is labeled as "Low-V Suboxic Detrital."

- Cluster 11: This chemical facies is highly enriched in Ca (3.99) with a very low Al (0.68). Thus, it is considered a limestone. Because high U (3.32), Zn (2.45) and Mn (2.43) and Mg (2.11) with a high Mo (1.71) are observed, the cluster is classified as euxinic. Cluster 11 is labeled as "Euxinic Lime."
- Cluster 12: This chemical facies is relatively high in Al (0.91) and Si (0.99) and relatively low in Ca (0.68). Thus it can be considered detrital. Because enrichment in Zn (2.95) and Mo (1.43) is observed, the cluster is considered euxinic. Cluster 12 is labeled as "Euxinic Detrital #1"
- Cluster 13: This chemical facies is relatively high in Al (1.00) and Si (1.05) and relatively low in Ca (0.69). Thus it can be considered detrital. Because average values of Cr (1.12) and Fe (0.93) are observed, the cluster is considered as suboxic. Cluster 13 is labeled as "Suboxic detrital."
- Cluster 14: This chemical facies is enriched in Al (1.12) and Si (1.18) and relatively low in Ca (0.52). Thus it can be considered detrital. Because high Mo (1.30) and Mg (1.75) are observed, the cluster is classified as euxinic. Cluster 14 is labeled as "Euxinic Detrital #2." It is chemically different from Cluster 12 because it is highly enriched in Mg. In contrast, Cluster 12 has very low Mg, too low to be detected.
- Cluster 15: This chemical facies is high in Al (1.02) and Si (1.23) and relatively low in Ca (0.67). Thus it can be considered detrital. Because strong enrichment in P (1.83) is observed, the cluster is classified as phosphatic. Cluster 15 is labeled as "Phosphatic Detrital."

Figure 20 represents the progression and evolution of chemical facies through the stratigraphic progression. It is obtained after bulk chemistry evaluation and after ordering of the clusters in a way allowing to move through the strata. This figure represents the redox signatures of each cluster. It also displays the labels of each cluster. After the

ordering of the clusters, redox signatures are highlighted and are easier to study and visualize on the graph. According to the distribution of the different clusters, the graph was divided into three main sections representing the evolution of the formation:

The first section is represented by a yellow background. It extends from the depths 11,370 ft to 11,110 ft. The main factor controlling this section is redox conditions and mineralogy. Clusters 4, 5, 9 and 15 are dominated by phosphate. Phosphate is the main controlling factor in these chemical facies. They mostly appear between depths 11,300 ft and 11,110 ft.

The second section is represented by a light brown background.. It extends from the depths 11,110 ft to 11,065 ft. It is dominated by clusters 2 and 6. These two clusters are similar in having both high Mg and high Ca (Table 4.a.). Cluster 13 also makes an appearance in this section, but is not exclusively showing at those depths. This section could represent a transition phase.

The third section is represented by a light red background.. It extends from depths 11,065 ft. to 10,900 ft (the end of the core). It is dominated by clusters 3 and 10. These clusters appear only in this section. They can be classified as the Bossier facies. Most of the Haynesville facies do not appear in the Bossier facies. However,some of the clusters (1, 11 and 6) make a small appearance in the upper part of the core corresponding to the Bossier. The total amount of sample from the Haynesville showing in the Bossier is less than 1%.

A surface boundary was placed at depth 11,300 ft. At this depth, cluster 7 stops dominating and the major clusters present become 8, 13, 12, 4, 5 and 9. Cluster 8 starts before the boundary but is dominating after it. Clusters 13, 12, 4, 5 and 9 start appearing after the sequence boundary at 11,300 ft.

Figure 21 displays the chemostratigraphic graphs of P, Ca, Zn and Mo, aligned with the HCA. It allows a comparison of the variations at different depths in both the chemical stratigraphy and the HCA clusters. Between depth 11,370 f. and 11,300 ft, a fluctuation is observed across all the chemostratigraphy graphs of P, Ca, Zn, and Mo. Between 11,300 ft and 11,110 ft, the chemostratigraphy graphs of P, Ca, Zn, and Mo display a high-frequency oscillating trend with a general increase in their content. This corresponds to the data in the HCA graph, where the clusters dominating are clusters 4, 5 and 9 (controlled by phosphate), as well as 8 (anoxic marl), 13 (suboxic detrital), 1 (Suboxic Dolomite) and 12 (Euxinic Detrital #1?). The values of phosphate increase, especially between depths 11,200 ft and 11,150 ft. These are the depths where the distribution of phosphate is the highest in the HCA graph. At depth 11,065, a large increase in Zn is observed, corresponding to clusters 3 and 10 in the HCA graph.

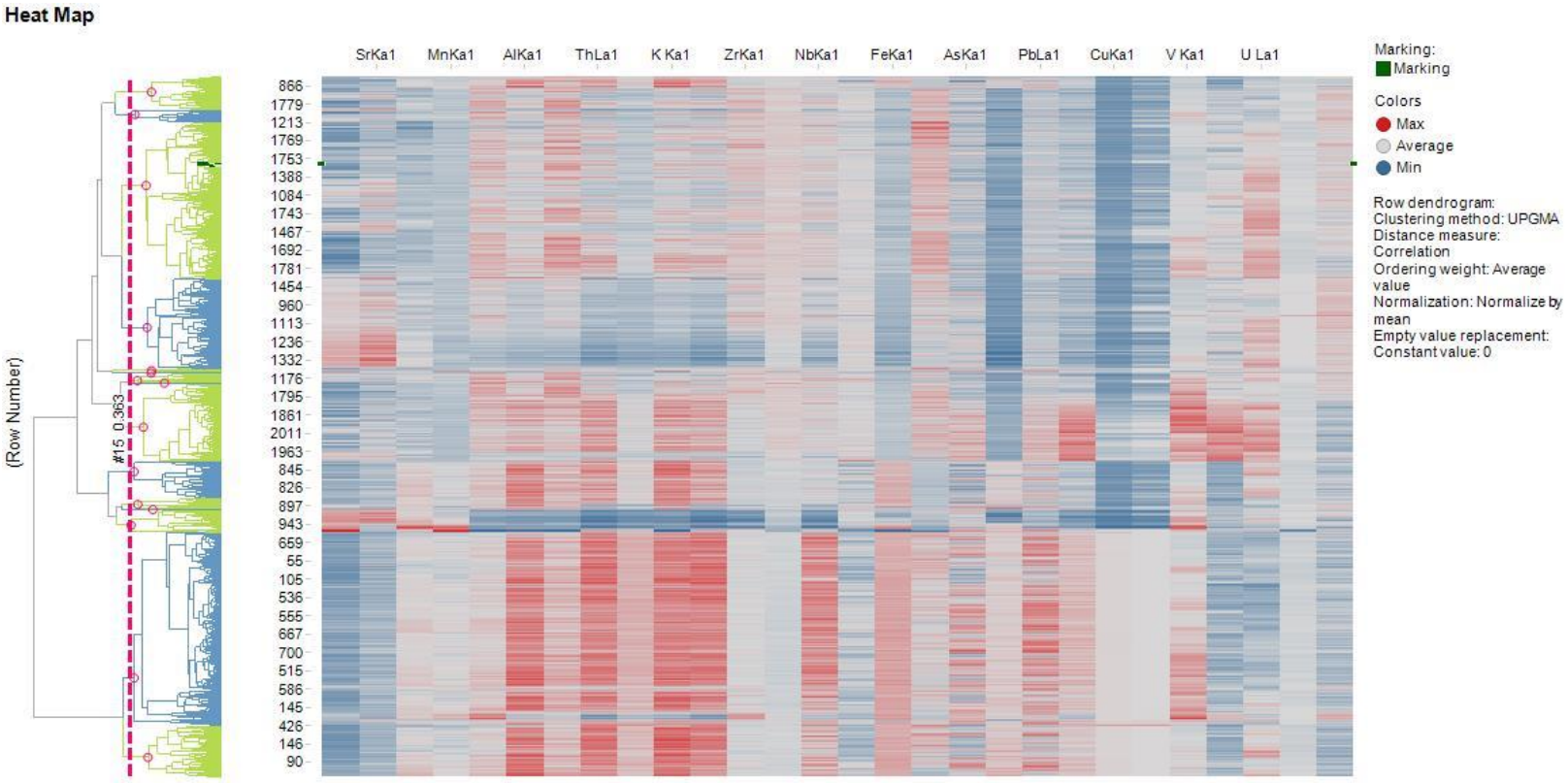

Figure 18: HCA heat map generated by Spotfire software showing chemical distribution of the 15 different clusters.

Cluster	1	Cluster	2	Cluster	3	Cluster	4	Cluster	5	Cluster	6	Cluster	7
n=	66	n=	106	n=	560	n=	37	n=	25	n=	32	n=	225
%Mg	4.98	%Mg	2.54	Zn (ppm)	2.68	V (ppm)	1.52	%P	2.09	%Mg	2.27	Mo (ppm)	3.87
%Ca	4.87	U (ppm)	2.00	Cu (ppm)	2.64	%P	1.35	U (ppm)	1.92	Co (ppm)	1.98	V (ppm)	3.51
V (ppm)	2.67	Co (ppm)	1.34	V (ppm)	1.78	%Ca	1.21	V (ppm)	1.80	V (ppm)	1.58	U (ppm)	2.80
%Mn	2.10	%Fe	1.20	%Mg	1.77	Y (ppm)	1.19	%S	1.47	%Fe	1.20	Ni (ppm)	1.26
Sr (ppm)	1.55	%K	1.14	Co (ppm)	1.50	Cr (ppm)	1.16	Cr (ppm)	1.25	%Al	1.11	Cr (ppm)	1.18
As (ppm)	1.07	%Al	1.14	%Fe	1.29	Zr (ppm)	1.07	Y (ppm)	1.14	%K	1.07	%S	1.17
Y (ppm)	0.97	Th (ppm)	1.09	Ga (ppm)	1.27	%S	1.06	Zr (ppm)	1.11	%S	1.07	As (ppm)	1.16
%S	0.95	Rb (ppm)	1.09	As (ppm)	1.26	%Na	1.06	%Si	1.10	%Ti	1.03	Th (ppm)	1.06
Co (ppm)	0.93	Ga (ppm)	1.05	Pb (ppm)	1.16	Sr (ppm)	1.04	%Ti	1.07	Y (ppm)	1.03	Rb (ppm)	1.05
%Fe	0.86	%Ti	1.05	Rb (ppm)	1.15	%Si	1.04	%Ca	1.02	%Si	1.01	%K	1.05
Pb (ppm)	0.84	%Mn	1.04	Ni (ppm)	1.13	%Ti	1.02	Sr (ppm)	1.02	%Mn	1.00	Pb (ppm)	1.04
%Na	0.75	%Si	1.03	%Al	1.13	Nb (ppm)	0.93	Nb (ppm)	1.00	As (ppm)	0.99	%Na	1.04
Ni (ppm)	0.73	Pb (ppm)	0.98	Nb (ppm)	1.13	%Mn	0.91	%Na	0.96	Pb (ppm)	0.98	%Si	1.04
Zr (ppm)	0.65	Nb (ppm)	0.96	%K	1.13	Mo (ppm)	0.91	%Al	0.95	Rb (ppm)	0.96	%Ti	1.03
Nb (ppm)	0.61	Zr (ppm)	0.95	Th (ppm)	1.12	%Al	0.89	Mo (ppm)	0.95	Th (ppm)	0.96	%Al	1.02
Th (ppm)	0.56	%S	0.93	%Mn	1.10	Pb (ppm)	0.86	%K	0.93	Ga (ppm)	0.95	Zr (ppm)	0.99
Ga (ppm)	0.55	Y (ppm)	0.91	%Ti	1.05	%K	0.86	Pb (ppm)	0.92	Ni (ppm)	0.94	Nb (ppm)	0.99
Rb (ppm)	0.53	Ni (ppm)	0.90	%Si	1.03	Rb (ppm)	0.85	Th (ppm)	0.91	Sr (ppm)	0.92	Ga (ppm)	0.97
Mo (ppm)	0.51	Cr (ppm)	0.88	Zr (ppm)	1.01	Th (ppm)	0.85	%Mn	0.91	Zr (ppm)	0.90	Sr (ppm)	0.95
%Si	0.50	Sr (ppm)	0.86	%Na	1.00	Ni (ppm)	0.83	Rb (ppm)	0.90	Nb (ppm)	0.88	Y (ppm)	0.93
%Ti	0.49	%Na	0.82	Y (ppm)	0.92	As (ppm)	0.83	Ni (ppm)	0.87	%Ca	0.86	%Mn	0.85
%P	0.46	As (ppm)	0.74	%S	0.87	%Fe	0.78	Ga (ppm)	0.83	%Na	0.84	%Fe	0.85
%Al	0.46	%Ca	0.66	Cr (ppm)	0.84	Ga (ppm)	0.78	%Fe	0.78	Cr (ppm)	0.82	%Ca	0.83
Cr (ppm)	0.44	%P	0.38	Sr (ppm)	0.82	Co (ppm)	0.54	%Mg	0.73	%P	0.68	Zn (ppm)	0.77
%K	0.39	V (ppm)	0.13	%P	0.57	Zn (ppm)	0.22	As (ppm)	0.65	Cu (ppm)	0.10	%P	0.66
U (ppm)	0.34	Mo (ppm)	0.02	%Ca	0.54	%Mg	0.21	Co (ppm)	0.50	Mo (ppm)	0.01	Co (ppm)	0.62
Cu (ppm)	0.10	Cu (ppm)	-0.01	Mo (ppm)	0.35	Cu (ppm)	0.05	Zn (ppm)	0.17	Zn (ppm)	-0.06	Cu (ppm)	0.53
Zn (ppm)	-0.30	Zn (ppm)	-0.20	U (ppm)	-1.22	U (ppm)	-0.72	Cu (ppm)	0.06	U (ppm)	-0.73	%Mg	0.08

Table 4 (a): HCA elemental ranking (Clusters 1-7)

Cluster	8	Cluster	9	Cluster	10	Cluster	11	Cluster	12	Cluster	13	Cluster	14	Cluster	15
n=	455	n=	259	n=	148	n=	5	n=	10	n=	94	n=	3	n=	5
U (ppm)	2.52	%P	3.69	Cu (ppm)	2.47	%Ca	3.99	Zn (ppm)	2.95	Cr (ppm)	1.12	%Mg	1.75	V (ppm)	3.81
Cr (ppm)	1.20	%Ca	2.17	Zn (ppm)	1.97	U (ppm)	3.32	Mo (ppm)	1.43	Y (ppm)	1.08	Mo (ppm)	1.30	%P	1.83
Mo (ppm)	1.13	U (ppm)	1.68	Co (ppm)	1.91	Zn (ppm)	2.45	Cr (ppm)	1.25	Zr (ppm)	1.06	%Si	1.18	%Mg	1.75
%Na	1.09	Sr (ppm)	1.52	%Mg	1.91	%Mn	2.43	%Na	1.14	%Ti	1.05	%K	1.15	Cr (ppm)	1.60
Zr (ppm)	1.08	Y (ppm)	1.18	U (ppm)	1.70	%Mg	2.11	Y (ppm)	1.09	%Si	1.05	Y (ppm)	1.15	U (ppm)	1.50
Y (ppm)	1.06	%S	1.15	%Fe	1.27	Co (ppm)	1.86	Zr (ppm)	1.03	%S	1.01	Cr (ppm)	1.14	%Si	1.23
%S	1.05	Cr (ppm)	1.04	Ga (ppm)	1.22	Cu (ppm)	1.72	%Ti	1.03	%K	1.01	%Al	1.12	Y (ppm)	1.10
%Si	1.04	Mo (ppm)	0.98	%K	1.19	Mo (ppm)	1.71	%Si	0.99	%Na	1.00	Zr (ppm)	1.12	Zr (ppm)	1.05
%Ti	1.04	%Na	0.96	Rb (ppm)	1.17	As (ppm)	1.46	Ni (ppm)	0.98	%Al	1.00	%Ti	1.08	Zn (ppm)	1.04
Nb (ppm)	0.99	Zr (ppm)	0.94	Th (ppm)	1.16	Pb (ppm)	1.25	Nb (ppm)	0.96	Rb (ppm)	0.99	%S	1.08	%Mn	1.03
Sr (ppm)	0.99	As (ppm)	0.90	%Al	1.15	Ga (ppm)	1.08	%S	0.96	Th (ppm)	0.98	As (ppm)	1.01	%S	1.03
%K	0.97	%Si	0.90	Ni (ppm)	1.09	Zr (ppm)	1.05	Rb (ppm)	0.96	Nb (ppm)	0.98	Nb (ppm)	1.01	%Ti	1.02
Th (ppm)	0.97	Nb (ppm)	0.87	Nb (ppm)	1.06	Ni (ppm)	1.05	U (ppm)	0.96	%Mn	0.94	Pb (ppm)	1.00	%Al	1.02
Rb (ppm)	0.96	Pb (ppm)	0.87	Pb (ppm)	1.05	Th (ppm)	1.02	Th (ppm)	0.95	%Fe	0.93	Rb (ppm)	0.97	%K	0.98
%Al	0.95	%Mn	0.86	%Ti	1.05	Rb (ppm)	1.01	%K	0.95	Ga (ppm)	0.93	Th (ppm)	0.96	Nb (ppm)	0.96
Pb (ppm)	0.91	%Ti	0.86	As (ppm)	1.04	Nb (ppm)	0.99	Sr (ppm)	0.92	Pb (ppm)	0.92	%Na	0.96	Th (ppm)	0.93
Ni (ppm)	0.90	Ni (ppm)	0.81	%Mn	1.02	Sr (ppm)	0.98	%Al	0.91	Sr (ppm)	0.90	V (ppm)	0.96	Rb (ppm)	0.93
Ga (ppm)	0.88	%Al	0.80	%Si	1.02	Y (ppm)	0.97	Pb (ppm)	0.91	Ni (ppm)	0.88	%Mn	0.94	%Fe	0.92
%Mn	0.87	Th (ppm)	0.76	%Na	0.99	%S	0.94	Ga (ppm)	0.88	Co (ppm)	0.84	Ni (ppm)	0.93	Pb (ppm)	0.92
%Fe	0.81	%K	0.74	Zr (ppm)	0.98	%Ti	0.83	%Mn	0.84	As (ppm)	0.80	Ga (ppm)	0.89	As (ppm)	0.91
As (ppm)	0.77	Rb (ppm)	0.73	Cr (ppm)	0.87	%Fe	0.77	As (ppm)	0.84	%Ca	0.69	Zn (ppm)	0.87	Sr (ppm)	0.90
%Ca	0.72	Ga (ppm)	0.71	Y (ppm)	0.85	%Na	0.76	%Fe	0.83	%P	0.62	%Fe	0.84	Ni (ppm)	0.87
%P	0.64	%Fe	0.71	Sr (ppm)	0.80	%Al	0.68	Co (ppm)	0.74	Mo (ppm)	0.39	Sr (ppm)	0.74	Co (ppm)	0.84
Co (ppm)	0.56	%Mg	0.59	%S	0.79	%K	0.66	%Ca	0.68	%Mg	0.36	Co (ppm)	0.67	Ga (ppm)	0.83
V (ppm)	0.14	Co (ppm)	0.43	%Ca	0.47	%Si	0.61	Cu (ppm)	0.66	Cu (ppm)	-0.01	%Ca	0.52	%Na	0.80
Zn (ppm)	0.07	Zn (ppm)	0.11	V (ppm)	0.43	Cr (ppm)	0.23	%P	0.29	Zn (ppm)	-0.17	%P	0.44	Mo (ppm)	0.73
Cu (ppm)	0.06	Cu (ppm)	0.04	%P	0.38	%P	-0.93	V (ppm)	-0.01	U (ppm)	-0.21	U (ppm)	0.38	%Ca	0.67
%Mg	-0.35	V (ppm)	-0.53	Mo (ppm)	0.23	V (ppm)	-7.01	%Mg	-0.70	V (ppm)	-0.81	Cu (ppm)	0.27	Cu (ppm)	0.20

Table 4 (b): HCA elemental ranking (Clusters 8-15)

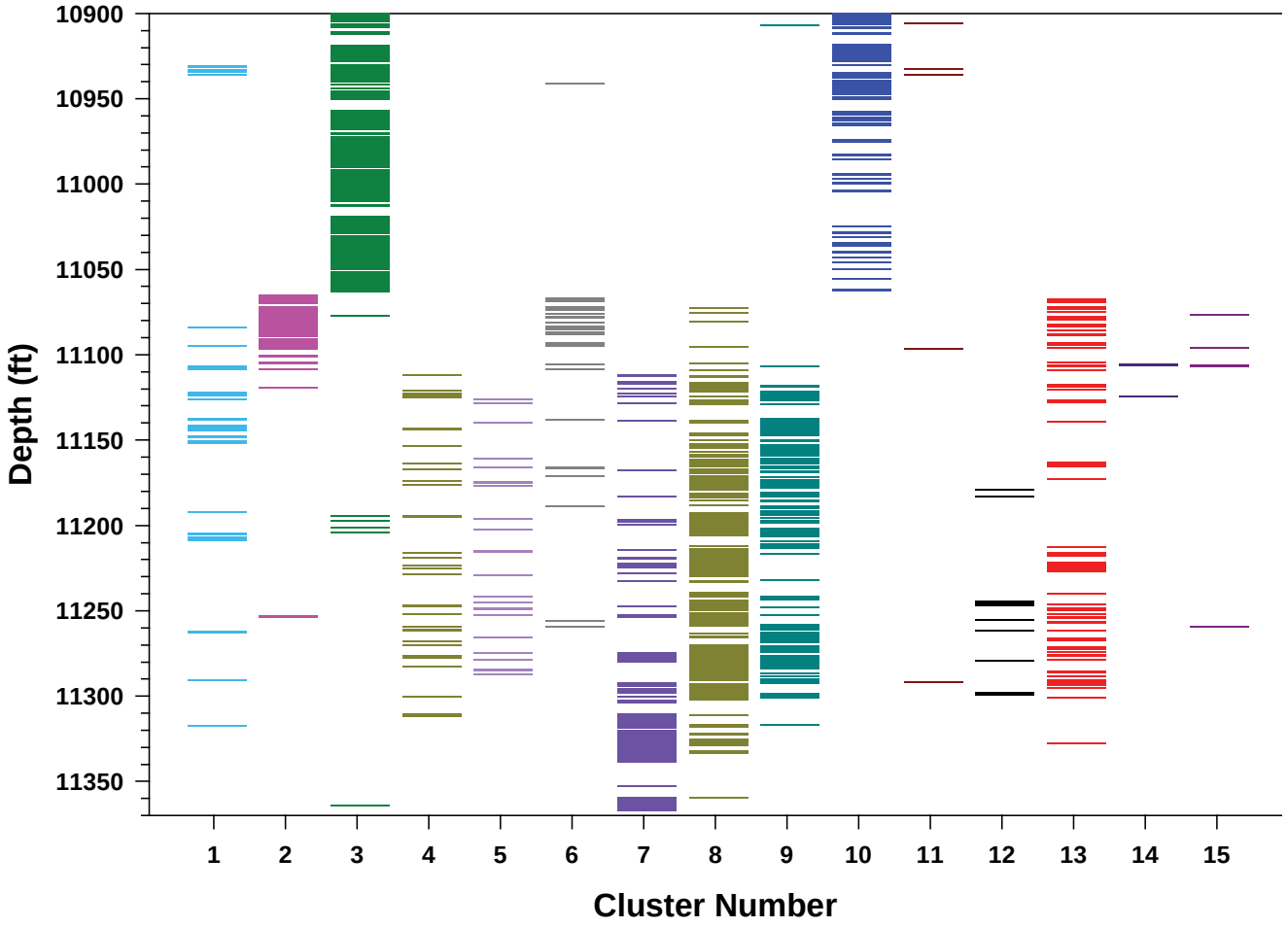

Figure 19: Cluster stratigraphy graph showing the distribution of the 15 clusters along the depth of the core.

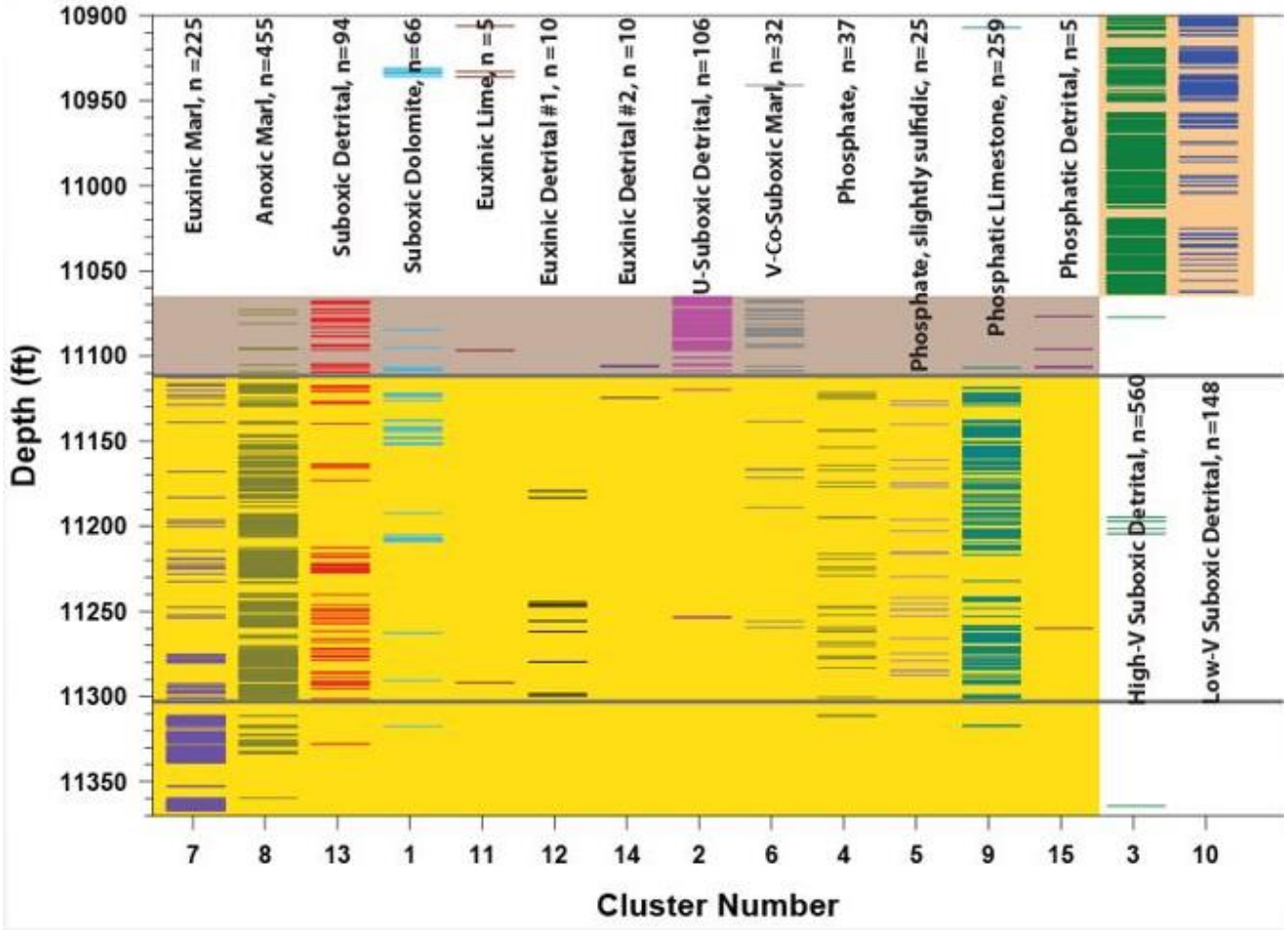

Figure 20: Cluster stratigraphy graph with ordered clusters showing the formation's evolution

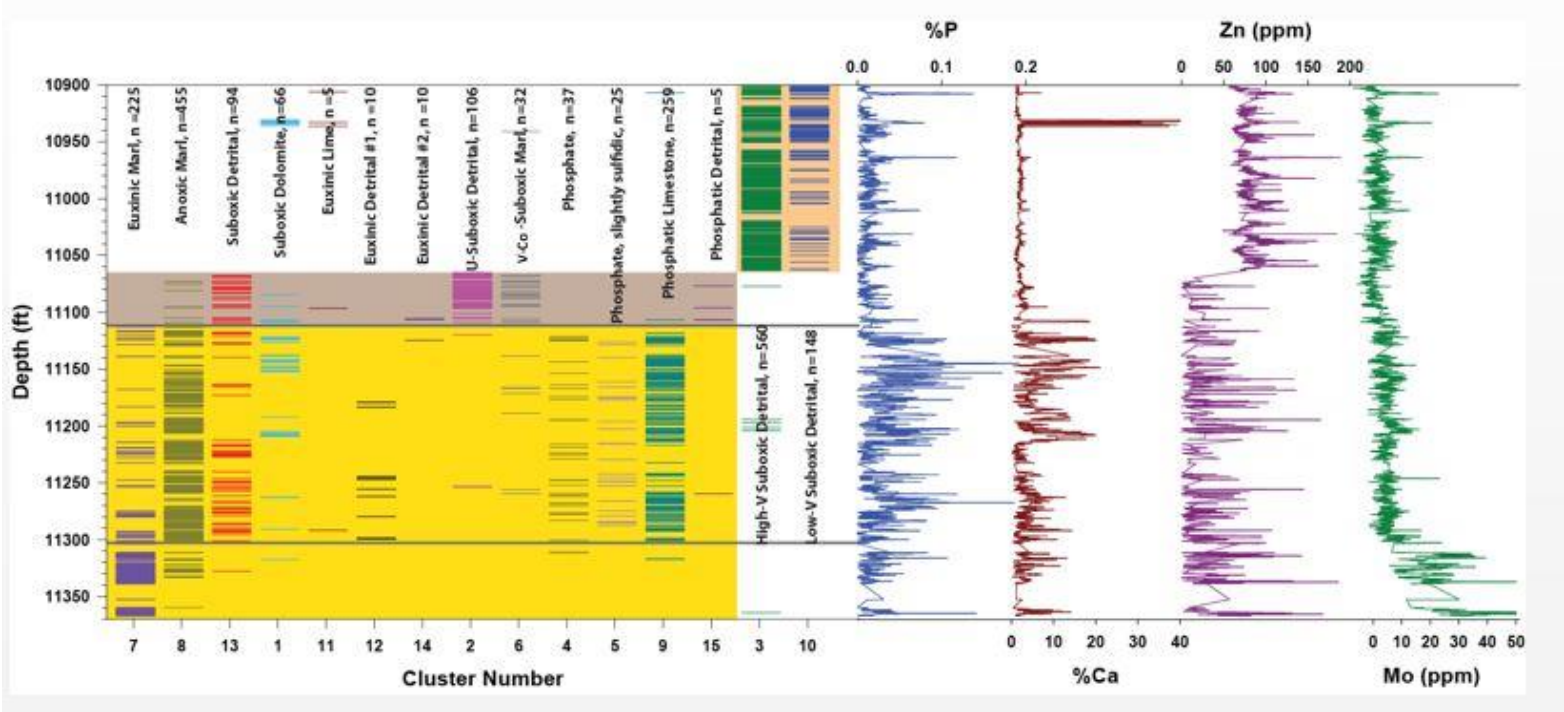

Figure 21: Hierarchical Cluster Analysis graph aligned with the chemical stratigraphy of P, Ca, Zn and Mo.

Cluster number	1	2	3	4	5	6	7
Characteristics	Suboxic Dolomite	U-Sub-oxic Detrital	High-V Sub-oxic Detrital	Phosphate	Phosphate, slightly sulfidic	V-Co-Suboxic Marl	Euxinic Marl
8	9	10	11	12	13	14	15
Anoxic Marl	Phosphatic Limestone	Low-V Sub-oxic Detrital	Euxinic Lime	Euxinic Detrital #1	Suboxic Detrital	Euxinic Detrital #2	Phosphatic Detrital

Table 5: Summary of clusters with labels based on their chemical distribution

Chapter 4: Discussion

The aim of this discussion is to interpret the geochemical data and chemostratigraphic variations in the T. W. George core in order to provide a better understanding of relative sediment contributions (siliciclastic/calcareous inputs), depositional environment, paleo-productivity, and sequence stratigraphy of the Haynesville.

1. Relative Sedimentary Contribution

1.1. Detrital Influx

The Si/Al ratio is generally assumed to represent the quartz/clay ratio in most mudrock environments (Tribovillard et al., 1994; Caplan and Bustin, 1998; Murphy et al., 2000Sageman, 2003; Rimmer et al., 2004). This assumption is supported by the XRD mineralogy data from the core (Figure 8 (a)). Here, more specifically, it is used as a proxy for relative mineralogical abundance of two different types of detrital influx, as biogenic silica has not been demonstrated to be a dominant phase in the Haynesville succession (Hammes et al., 2011). Moreover, silicon displays a well-defined linear trend with aluminum (Figure 9), suggesting that most of the silicon in the succession is supported in the clay fraction. Low Si/Al values occur between the bottom of the core and 11,320 ft. The Si/Al ratio increases at around 11,320 ft until 11,063 ft. At 11,063 ft to the top of the core, the Si/Al ratio decreases again. However, overall, the Si/Al cross-plot and the lack of a well-defined SiO2 end-member on the Ca-Al-Si ternary indicate that quartz plays less of a role in the Haynesville succession relative to calcite (as proxied by %Ca) and clay (as proxied by %Al).

In general, because of their high valence-to-radius ratio, Ti and Zr are terrestrially derived elements that are not readily soluble in water. Thus, peaks of Si along with peaks of Ti and Zr at the same stratigraphic depth also indicate the detrital origin of the quartz in the depositional system. Some high silicon data points plot above the silicon-aluminum trend line (Figure 9), which indicates the presence of different silica minerals besides clay. Abrupt peaks of Si/Al can be also identified in Figure 12. These peaks of silica and silica normalized to clay (Si/Al), observed in Figures 9 and 12, probably represent quartz influx to the basin within a very short period of time. This abrupt influx may indicate detrital input through aeolian processes, flooding events, winnowing of the clay fraction, and/or turbidites. The cluster analysis results, summarized in Table 4 (a) and (b), also show chemical facies that are enriched in Si (clusters 5, 13, 14 and 15). The XRD results (Figure 8 (a)) indicate the presence of a significant amount of quartz, and much less albite.

A general assumption made in most mudrock studies is that aluminum is usually detrital and is unaffected by diagenesis or biological processes (Brumsack, 2006; Tribovillard et al., 2006). This is thought to be the case because of the high valence-to-radius ratio. The cross-plots of the six different elements—Si, K, Ti, Ca, Ga, and Th with aluminum—display the detrital provenance in the rock (Figure 9). Elements that show linear relationships with Al are generally thought to be of detrital origin (Calvert et al., 2007; Piper and Calvert, 2009). A linear trend is observed between Si, Ti, K, Ga, Th and Al with a positive slope. Silicon, Ti, K, Ga, and Th are of detrital origin.

High Al values were observed at the bottom of the core, between the depths 11,367 ft and 11,320 ft, and have an average value of 6.7%. Aluminum values decrease at around depth 11,320 ft to depth 11,063 ft with values averaging 5.8 %. Around depth 11,063 ft up to the top of the core, Al values increase again with an average value of 7.3 % (Figure 12). This indicates a higher clay content in the upper section of the core.

On the cross-plot showing %Fe vs. %Al (Figure 10), we observe a linear trend between the two elements. This indicates that Fe, like Al, is largely of detrital origin and is present in clay. Some data points on the cross-plot are above the Fe-Al line, which shows an enrichment in Fe and its presence in other minerals besides clay. Fe is most probably present in the mineral illite, as observed by XRD analysis (Figure 8 (a)) but it is also held within the pyrite mineral phase. Thus, because Fe is partitioned between several minerals, it is of less use in defining mineralogical trends in the Haynesville succession. This geochemical interpretation using a quantitative approach divides the core into three different lithostratigraphic units, the lower Haynesville, the upper Haynesville and Bossier.

1.2.Calcareous Phase Analysis

The Ca-rich lower Haynesville grades into the more Ca-rich upper Haynesville, then into the Ca-poor Bossier, as is reflected in the chemostratigraphy (Figure 12). The XRD data (Figure 8 (a)) demonstrate that calcite is the dominant calcium-bearing mineral phase in the Haynesville Formation. This is further demonstrated by the bulk elemental mineralogy trend in the calcium versus calcite plot in Figure 16.

Low Ca values were observed at the bottom of the core, between the depths of 11,367 ft and 11,320 ft, with an average content of 3.5%. Ca values increase in the depth interval between 11,320 ft to 11,063 ft, with an average content of 4.8%. Around 11,063 ft upward to the top of the core (10,900 ft), which is dominated by Bossier Formation strata, Ca values decrease again and are the lowest recorded, with an average content of 2.6%. A few outliers are present in a very small depth interval between 10,930 ft and 10,936 ft, showing abnormal recording of elemental concentrations. This is observed in the same eight samples with all the elements. These samples show very low %Al (as low as 0.03 %)

and %Fe (as low as 0.68 %), and very high values of %Ca (as high as 40.4%) and %Mn (as high as 0.14 %).

The cross-plots showing elemental content %Mg, %Fe, %Mn, %K and %Si vs. %Ca, as well as Sr content in ppm vs. %Ca (Figure 11), depict the elements present in the calcareous phase. Note the very low %Ca (%0 to %2) in a group of samples on all the cross-plots, which corresponds to the detrital phase. A negative trend in the plot of %K vs. %Ca indicates that calcite dilutes the dominant potassium-bearing phase(s), such as feldspars and clays. This is also demonstrated to be true of the Si-Ca relationship. The relationship is less clear in the Fe-Ca plot, suggesting that only one mineral phase can contain both Fe and Ca. Positive relationships occur in the Mg-Ca plot and the Mn-Ca plot. Finally, the Sr-Ca relationship is also positive. Mn variation across the core was observed in Figure 12; between the bottom of the core and 11,320 ft, Mn values are the lowest, with an average value of 0.0189 %. At 11,320 ft Mn content increases up to depth 11,063 ft, with an average of 0.0197 %. Around 11,063 ft upward to the top of the core, there is a further increase in Mn content, reaching its highest values recorded in the core, with an average of 0.0256 %.

The mineralogy shown in Figure 8 (a) displays relationships with the major element variations depicted in Figure 12: From the bottom of the core to around depth 11,300 ft, we observe a relatively equal distribution in the mineral phases, with no particular mineral dominating. Between 11,300 ft and 11,230 ft, calcite percentage increases in the core, illite and kaolinite decrease slightly in percentage, quartz is relatively constant, and albite, dolomite and pyrite percentages are also relatively the same. Between 11,230 ft and 11,150 ft, a further increase in calcite occurs, relative to the underlying package and there are further decreases in illite, kaolinite, quartz, and a relatively stable percentages of albite, dolomite and pyrite. Between 11,150 ft and 11,115 ft is the highest increase in calcite,

reaching highest values between 65% and 70%. Illite, kaolinite and quartz further decrease in content and reach their lowest values in the core. Albite, dolomite and pyrite are still relatively at the same percentages. Between 11,115 ft and 11,105 ft, the lowest calcite percentage is and a peak in dolomite occur, with the highest percentage of dolomite reaching nearly 70%. Illite, kaolinite, quartz and albite have very low percentages in that section of the core. Pyrite content remains relatively the same. Between 11,105 ft and the top of the core, increases in illite, kaolinite and quartz appear, reaching their highest content in this top part of the core. Calcite decreases in mineral percentage to between 20% and 30%. Albite, dolomite and pyrite have again the same percentages as in the bottom part of the core.

2. DEPOSITIONAL ENVIRONMENT OF THE HAYNESVILLE

The deposition environment of the Haynesville was studied in this thesis by interpreting the changes in chemostratigraphy within the T. W. George core. Redox-sensitive trace elements were used to evaluate paleoenvironments. Molybdenum, Cr, U and V are more soluble in oxidizing conditions and less soluble in reducing conditions. Thus, they are enriched and found in anoxic sediments (Tribovillard et al., 2006). The Ca-Al-Si ternary diagram (Figure 15) shows that the Haynesville is relatively clay rich in the eastern part of the East Texas Basin, which suggests that the East Texas Basin deepens toward the east.

Si, Zr, Ti are detrital proxies (Figure 14). Peaks of Si are observed in the depth interval 11,110 ft and 11,120 ft, as well as in the depth interval 11,220 ft and 11,240 ft. At these same depth intervals, we observe elevated amounts of Ti and Zr. The elements Si, Ti and Zr are co-varying across the core. Given that the peaks of Si are at the same depth

intervals as the peaks of Zr and Ti, this confirms the presence of detrital silica, because Ti and Zr are detrital elements. In heavy minerals (rutile for example), Ti exists, which substantiates a high- energy coastal depositional environment (Dellwig et al., 2000). These data indicate that the Haynesville was deposited under a highstand of low energy and in a deeper depositional system. In contrast, the silt-rich Bossier was deposited under a lowstand high- energy and shallow depositional system.

Fe is an anoxia indicator normalized to clay (Figure 10). In Figure 12, between the depths 11,367 ft and 11,320 ft, Fe values have an average of 3.1 %. In the depth interval 11,320 ft and 11,063 ft, we observe a slight decrease in Fe content with an average of 2.9 %. Around 11,063 ft upward to the top of the core, a clear increase in Fe content occurs, the highest recorded in the core, with an average of 4.6 %. A high Fe content indicates anoxic conditions during deposition.

Mo and V (Figure 13), are also anoxia indicators and redox-sensitive trace elements. They are enriched in anoxic sediments because of their higher solubility in oxidizing conditions and lower solubility in reducing conditions (Tribovillard et al., 2006; Calvert et al., 2007). A high Mo content indicates the presence of an anoxic environment. High Mo levels are observed in the Haynesville Formation, the highest levels being in the lower Haynesville (Figure 13). Between depths 11,367 ft and 11,320 ft, we see a high Mo content with an average content of 23 ppm and values reaching as much as 59 ppm. Between depths 11,320 ft and 11,090 ft, a lower Mo content with an average content of 5 ppm appear. Around 11,090 ft to the top of the core, Mo content decreases further, with an average content of 1 ppm, and many samples have Mo values too low to detect. The high Mo concentrations observed at the bottom of the core, corresponding to the lower Haynesville, indicate dysoxic and anoxic conditions during deposition. On the other hand, Mo enrichment is not recorded in the overlying parts of the core (1 ppm and 5 ppm),

confirming the prevalence of more oxygenated conditions during deposition, corresponding to the Bossier Formation.

The trace elements V and Zn also have a strong affinity toward anoxia-euxinia (Algeo et al., 2003; Algeo and Maynard, 2008). Between depths 11,367 ft and 11,320 ft, a high V content is observed with an average of 42 ppm and a maximum of 107 ppm. From depth 11,320 ft and upward, irregular variations with relatively low V content are observed, with an average of 4 ppm. At 11,063 ft upward to the top of the core, we see a relative increase in V content with irregular fluctuations ranging from values as low as 0ppm to as values as high as 107 ppm with an average content of 15 ppm (Figure 13). For the element Zn, between the bottom of the core and 11,320 ft, the Zn average content is 34 ppm. Low Zn values are observed from 11,320 ft to 11,063 ft, as low as 0 ppm with occasional increases and an average value of 5 ppm (Zn values are too low to be detected in some samples). An increase in Zn content, reaching its highest values, starts at around 11,063 ft upward to the top of the core, with an average content of 68 ppm (Figure 13). These variations indicate that anoxic conditions turned dysoxic in the East Texas Basin during the Kimmeridgian.

A high sulfur content is observed in the lower part of the core, corresponding to the lower Haynesville. The overlying parts of the core record a lower sulfur content. They correspond to the upper Haynesville and Bossier Formation (Figure 14). This confirms a depositional environment that was anoxic to dysoxic during the Late Jurassic when this formation was deposited.

3. PALEO-PRODUCTIVITY OF THE HAYNESVILLE

Nutrients from terrestrial origins that are delivered to the ocean lead to high surface water productivity. Having high productivity creates a rise in the demand for benthic

oxygen. Then bottom water becomes an anoxic environment (Algeo et al., 1995; Rimmer et al, 2004). Anoxic waters are the most suitable for organic matter preservation (Demaison and Moore, 1980). Thus, productivity has a direct relation to the accumulation and preservation of organic matter. Since total organic carbon in sediments is the residue of past biota, sediments with high TOC were deposited in anoxic water, and they indicate high productivity. An elevated input of organic matter in the water column is crucial for maintaining oxygen depletion, and thus an anoxic environment.

Upwelling can also lead to high productivity (Piper and Perkin, 2004). Upwelling is a wind-driven oceanographic phenomenon involving cooler, denser and more nutrient rich water moving toward the ocean surface and replacing the warmer, less dense and nutrient-depleted surface water. The Late Jurassic, being a warm interglacial geologic time, is characterized by large gaps in temperature between the ocean and the land. This can favor seasonal upwelling. Being rich in nutrients, the upwelled water favors the growth and reproduction of primary producers, leading to high productivity. Thus, the Late Jurassic is considered a time of high biologic productivity (Algeo et al., 2008).

From the bottom of the core up to depth 11,110 ft, the TOC values recorded are high and fluctuate between %2 and %4 (Figure 8 (b)). These relatively elevated levels of TOC in the lower part of the core (lower Haynesville) correspond to high Mo, low Zn and low As (Figure 13) and to high Si/Al trends and low Fe (Figure 12). These relationships indicate an increase in production during that time and the presence of biogenic silica (Sageman, 2002). Around depth 11,110 ft, a sharp decrease in TOC, to less than %1, is observed. This TOC level remains low up to the top of the core, indicating a decrease in production. This section of the core corresponds to the Bossier Formation that is characterized by a low organic matter preservation and productivity.

Oxygen depletion or anoxia along with high productivity lead to the high preservation of organic matter. The high level of TOC observed in the Haynesville Formation is caused by the high productivity and anoxic to euxinic water conditions. In contrast, the low level of TOC observed in the Bossier Formation is caused by a low productivity and oxic to dysoxic water conditions.

4. SEQUENCE STRATIGRAPHY OF THE HAYNESVILLE

Sequence stratigraphy links sedimentary deposits relative to sea-level changes and sediment supply and divides them into sequences separated by unconformities (Taylor and Sellwood, 2002). The Haynesville and Bossier formations were deposited in the Late Jurassic, within a global second-order transgression cycle during a time of rising sea level (Hallam, 1978, 2001; Goldhammer, 1998).

The following sequence stratigraphy section of this thesis links chemostratigraphy to sequence stratigraphy by using the chemostratigraphic data acquired, as well as by citing previous research on East Texas Basin sequence stratigraphy. It is not intended to be a detailed sequence stratigraphic analysis of the East Texas Basin or the Gulf of Mexico.

It is challenging to study sequence stratigraphy in mudrocks because of their fine grain nature and their homogeneous lithology (Ver Straeten et al., 2010). This is why a multi-proxy geochemical approach can be helpful in depicting the stratigraphic surfaces and system tracts. Because the T. W. George is proximal to the shelf, the principles of sequence stratigraphy are more valid to apply (Mainali, 2011). Sedimentary distribution in the East Texas Basin during the Jurassic was as follows: Siliciclastic deposition in the north and east parts, and carbonate production in the south and west (Goldhammer, 1998; Ewing, 2001, 2009; Hammes et al., 2011). Thus, Ca is a strong detrital indicator in the southern

and western parts of the basin, and Si is a more representative indicator of sedimentary content of the northern and eastern parts of the basin.

The Lower Haynesville facies were found to be calcareous, which was confirmed by Figures 9, 12 and Figure 8 (a), as previously shown. TOC-rich accumulations were found downslope and were produced in the deeper parts of the basin, driven by the sedimentary dynamics of the mass-wasting processes, as shown in Figure 8 (b). TOC accumulation is observed in the lower part of the core corresponding to the Haynesville Formation. The Bossier Formation, in contrast, was interpreted to have more clay rich facies with a lower calcareous and higher muddy composition. This interpretation is supported by the XRD analysis (Figure 8 (b)) and XRF (Figure 13) results, which show low Mo and V concentrations and low TOC accumulations, thus confirming a more oxygenated Bossier with lower productivity. High fluctuations of the element V (Figure 10) can be combined with cyclical fluctuations of Zr (Figure 11). This relationship was previously interpreted to indicate the occurrence of transgressive- regressive cycles, which is helpful when correlating in the Haynesville shale (Sano et al., 2013).

Because the Haynesville shows anoxic-dysoxic facies, as shown previously in the depositional environment section of this thesis, sedimentary proxies such as Mo and TOC can be used to outline sequence boundaries and sequence tracts. On the other hand, because the Bossier shows dysoxic-oxic clastic facies, as previously shown, proxies such as Si, and bioturbation are used to attempt to outline sequence boundaries and sequence tracts (Werne et al., 2002; Ver Straeten et al., 2002, 2010).

The geochemical proxies Si/Al (Figure 12), Al (Figure 12), TOC (Figure 8(b)) and bioturbation (Figures 6 and 7) are used to identify position within a sequence (Ver Straeten et al., 2002).

4.1.Highstand

Increased depth is usually interpreted to create more anoxic conditions. Multiple proxies can be used for deep water and highstand system tracts: hydrocarbon content, pyrite content, trace metals content like molybdenum and vanadium, and lithostratigraphic indications like laminations in the core. The presence of hydrocarbons in the Haynesville shale is displayed through TOC variations (Figure 8 (b)). Sea-level rise leads to TOC enrichment in shelf depositional environments such as those during the Kimmeridgian (Arthur and Sageman, 2004). Framboidal pyrite is another indication of anoxic conditions and increased depths (Hammes et al., 2011). The presence of pyrite is observed at the bottom of the core corresponding to the lower Haynesville (Figure 6). The core scans in Figure 7 (J) and Figure 7 (K) show mudstone facies with parallel-to-bedding-plane discontinuous pyrite-filled fractures at depth: 11,286 ft and 11,307 ft. Trace elements such as Mo and V can be used as indicators of deep-water anoxic conditions of a probable highstand system (Werne et al., 2002; Rimmer et al., 2004; Algeo and Lyons, 2006; Rowe et al., 2008). The high Mo concentrations observed at the bottom of the core correspond to the lower Haynesville, as previously shown, and indicate dysoxic and anoxic conditions during deposition and a probable highstand system tract. On the other hand, Mo enrichment is not recorded in the overlying parts of the core (1 ppm and 5 ppm), corresponding to the Bossier Formation, confirming the prevalence of more oxygenated conditions during deposition of the Bossier. Lithostratigraphic facies with laminations are observable in the core and are also indicators of a highstand system tract. Laminations in the T. W. George core are observed between 11,093 ft and 10,992 ft (Figure 6). The facies showing these laminations are displayed in the core scans in Figure 7 (C, D, E and F). These laminations indicate that the sediment was not destroyed by bioturbation. Thus, deep waters are interpreted to be present, allowing dominance of a highstand system tract. Because Mo,

TOC and anoxia relate chemically to each other, they can be used together to show eustatic rise (Sageman and Lyons, 2003; Tribovillard et al., 2006). TOC and the trace elements Mo and V show symmetrical cycles in Figure 8 (b) and Figure 12. Thus the Haynesville can be interpreted to have formed in a highstand system tract.

4.2.Lowstand

Clastic input is higher during lowstand because terrestrial input increases during lower sea levels driven by wind activities. A higher level of bioturbation is also more likely to be observed in shallow waters during lowstand system tracts (Loucks and Ruppel, 2007). As previously interpreted in the "Relative sedimentary input" section, %Al is usually used as a stratigraphic proxy for clay and Si/Al ratio as an indicator of quartz/clay. Thus, a high Si/Al ratio can be a proxy for a lowstand with a sand-dominated lithology. In the upper part of the core corresponding to the Bossier Formation, high %Al, Si/Al and low Mo and V are displayed, leading to the interpretation of the Bossier to have more clay rich facies with a lower calcareous, higher muddy character. Thus the Bossier can be considered to have been deposited during a lowstand system tract.

4.3.Maximum Flooding Surface (MFS)

The Haynesville is a second-order transgressive deposit capped by the maximum flooding surface (MFS) that marks the maximum extent of transgression (Goldhammer, 1998; Hammes et al., 2011). The duration of a second-order sequence extends from 10 to 80 Myr (Vail et al., 1977). In contrast, the chemostratigraphic cycles analyzed at a high resolution of 2-inch intervals, are of a higher order: this geochemical study of the T.W. George, the longest available Haynesville core (less than 400 ft), represents only 6-7 million years of deposition (Mainali, 2011). Thus the core does not cover the entire span of the second-order sequence, making the second-order MSF, unidentifiable in the analysis.

4.4.HCA Sequence Boundary Interpretations

Figure 19 shows the different clusters and their distribution across the depth of the core after HCA. Some of the clusters appear only in particular depths of the core. Each cluster is characterized by dominant elements that can be identified in Tables 4 (a) and 4 (b). The clusters were labeled according to their characteristics (Table 5). The clusters in Figure 19 were ordered in Figure 20 according to their characteristics and to their abundance in particular depths, showing the evolution of the formation.

Between depths 11,370 ft and 11,110 ft, in figures 20 and 21, the dominating clusters are: Cluster 7 (Euxinic marl), cluster 8 (Anoxic marl), cluster 13 (Suboxic detrital), cluster 1 (Suboxic dolomite) and cluster 12 (Euxinic detrital #1). Thus, the main factor controlling this section is redox conditions (yellow background). Cluster 7 (euxinic marl) is the main dominant cluster from 11,370 ft to 11,300 ft. This correlates with the high Mo displayed in Figure 21, confirming a euxinic character of the lower Haynesville. At 11,300 ft, cluster 7 stops dominating and the major clusters present become 8, 13, 12, 4, 5 and 9. Thus, a surface boundary was placed at depth 11,300 ft (Figure 20). Clusters 13, 12, 4, 5 and 9 start appearing after the sequence boundary at 11,300 ft. The depth interval (11,370 ft to 11,300 ft) could be interpreted as the lower Haynesville. This assumption is confirmed by the chemostratigraphic data from Figures 12 and 8 (a), and the TOC data in Figure 8 (b), as studied in the previous sections. A transition phase (light brown background) between the Haynesville Formation and the Bossier Formation is interpreted to have occurred in the depth interval (11,110 ft to 11,060 ft). The dominating clusters in this depth interval are cluster 2 (U-suboxic detrital) and cluster 6 (V-Co-suboxic marl). Cluster 13 (Suboxic detrital) is also present in this transitional phase. The Bossier Formation facies (light pink background) are characterized by two main dominating clusters: cluster 3 (High-V suboxic detrital) and cluster 10 (Low-V suboxic detrital). This correlates with low

Mo and Ca values (Figure 21), confirming a more oxygenated calcareous-rich Bossier Formation. A sequence boundary is placed at 11,060 ft, after the transitional phase and before the overlying Bossier Formation.

Chapter 5: Conclusions

Geochemical data, techniques and proxies were used to determine the Haynesville Formation's depositional system and sequence stratigraphy and the environmental and paleoceanographic conditions that existed during the Kimmeridgian Late Jurassic. Results of this analysis led to the following conclusions.

A. Silicon content is linked to clay content in the Haynesville Formation. Silicon is also present in minerals other than clay, mainly quartz. Iron content is also linked to clay content in the Haynesville Formation. Iron is also found in illite and pyrite.

B. Geochemical studies of the Haynesville complement previous lithostratigraphic studies and interpretations. Geochemical analyses show the composition and variations of the formation using a quantitative approach. Hierarchical cluster analysis (HCA) complements the geochemical studies by providing a statistical method for grouping the samples into different chemical facies.

C. The dominant conditions during the lower Haynesville deposition were anoxic euxinic. They became dysoxic toward the upper Haynesville, then they became more oxygenated when the Bossier strata were deposited. The degree of anoxia and the redox conditions are the main cause of the geochemical variations, especially in the lower Haynesville. This conclusion was confirmed mainly by the interpretation of iron, molybdenum, vanadium, zinc and TOC data and by the Hierarchal Cluster Analysis.

D. The Haynesville Formation, is rich in TOC, which indicates high productivity during the Kimmeridgian and the occurrence of biogenic silica. In contrast, the Bossier Formation was proven to be low in TOC and had low organic matter preservation and primary productivity.

E. The T.W. George core of Harrison County, East Texas comprises three major sections: a Ca-rich lower Haynesville that turns into a more Ca-rich upper Haynesville and then becomes a Si-rich and Ca-poor Bossier.

F. Sequence boundaries were placed at 11,300 ft after the lower Haynesville, at 11,110 ft before the transitional phase between the Haynesville and Bossier formations, and at 11,060 ft at the start of the Bossier Formation.

G. The greenhouse-like climate during the Late Jurassic led to the deposition of strata that now have great economic value. These petroleum source rocks include the mudrocks of the Haynesville Formation of the East Texas Basin.

Bibliography

Algeo, T.J., Schwark, Lorenz, Hower, J.C., 2003. High-resolution geochemistry and sequence stratigraphy of the Hushpuckney Shale (Swope Formation, eastern Kansas); implications for climate-environmental dynamics of the Late Pennsylvanian Midcontinent Seaway. Chemical Geology 206 (2004); 259–288.

Algeo, T.J., Lyons, T.W., 2006. Mo-total organic carbon covariation in modern anoxic marine environments: implications for analysis of paleoredox and paleohydrographic conditions. Paleoceanography, v. 21, PA1016, doi: 10.1029/2004PA001112.

Algeo, T.J., Lyons, T.W., Blakey, R.C., Over, D.J., 2007. Hydrographic conditions of the Devono-Carboniferous Seaway inferred from sedimentary Mo-TOC relationships. Paleogeography, Paleoclimatology, Paleoecology 256; 204–230.

Algeo, T.J., Maynard, J.B., 2008. Trace-metal covariation as a guide to water-mass conditions in ancient anoxic marine environments, Geosphere, V. 4; no. 5; 872–887.

Algeo, T., Rowe, H., Hower, J.C., Schwark, L., Herrmann, A., Heckel, P., 2008. Changes in ocean denitrification during Carboniferous glacial-interglacial cycles, Nature Geoscience Vol. 1. Macmillan Publisher Limited.

Algeo, T.J., Tribovillard, N., 2009. Environmental analysis of paleoceanographic systems based on molybdenum-uranium covariation. Chemical Geology. 268; 211–225.

Aller, R.C., 1994. Bioturbation and remineralization of sedimentary organic matter: effects of redox oscillation. Chemical Geology 114, 331–345.

Arthur, M.A., Sageman, B.B., 1994. Marine black shales: depositional mechanisms and environments of ancient deposits: Annual Review of Earth and Planetary Sciences, v. 22, p. 499–551.

Arthur, M.A., Sageman, B.B., 2005. Sea-level control on source-rock development: perspectives from the Holocene Black Sea, the mid-Cretaceous Western Interior Basin, and the late Devonian Appalachian basin. In: Harris, N.B. (Ed.), The Deposition of Organic-Carbon-Rich Sediments: Models, Mechanisms, and Consequences: Special Publication, vol. 82, pp. 35–59.

Berner, R.A., 1990. Atmospheric carbon dioxide levels over Phanerozoic time. Science, 249: 1382–1386.

Berner, R.A., 1992. Paleo-CO2 and climate. Nature 358: 114.

Berner, R.A., 1994. Geocarb II: A revised model of the atmospheric CO2over Phanerozoic time. American Journal of Science., 294; 56–91.

Blakey, R., Ranney, W., 2014. Ancient Landscapes of the Colorado plateau. Grand Canyon Geosystems, Inc.

Bojanowski, R. & Paslawska, S., 1970. On the occurrence of iodinc in bottom sediments and interstitial waters of the southcrn Bahic Sea. Acta (;eophysica Polemir'a 18. 277-286.

Boyle, E. A., 1983. Chemical accumulation variations under the Peru Current during the past 130000 years, J. Geophy. Res., 88, 7667– 7680.

Brumsack, H.J., 1989. Geochemistry of recent TOC-rich sediments from the Gulf of California and the Black Sea. Geologische Rundschau 78/3; 851–882.

Buller, D., Dix, M.C., 2009. Petrophysical evaluation of the Haynesville shale in northwest Louisiana and northeast Texas. Gulf Coast Association of Geological Societies Transactions 59, 127–143.

Calvert, S.E., Pedersen, T.F., 1993. Geochemistry of Recent oxic and anoxic marine sediments: implications for the geological record. Marine Geology 113; 67–88.

Calvert, S.E., Pedersen, T.F., 2007. Elemental proxies for palaeoclimatic and palaeoceanographic variability in marine sediments: interpretation and application. In: Hillaire-Marcel, C., Vernal, A.D. (Eds.), Proxies in Late Cenozoic Paleoceanography. Elsevier, Amsterdam.

Cicero, A.D., Steinhoff, I., McClain, T., Koepke, K.A., and Dezelle, J.D., 2010. Sequence stratigraphy of the Upper Jurassic mixed carbonate/siliciclastic Haynesville and Bossier shale depositional systems in east Texas and northern Louisiana: Gulf Coast Association of Geological Societies Transactions, V. 60; 133–148.

Crusius, J., Thomson, J., 2000. Comparative behavior of authigenic Re, Mo and U during reoxidation and subsequent long-term burial in marine sediments. Geochimica et Cosmochimica Acta 64, 2233–2242.

Demko, T.M., Parrish, J.T., 1998. Paleoclimatic setting of the Upper Jurassic Morrison Formation. Modern Geology 22, 283–296

Ewing, T.E., 2001. Review of Late Jurassic Depositional System and Potential Hydrocarbon Plays, Northern Gulf of Mexico Basin, Gulf Coast Association of Geological Societies Transactions, Volume 51, 2011.

Froelich, P. N., Klinkhammer, G. P., Bender, M. L., Luedtke, N. A., Heath, G. R., Cullen, D., Dauphin, P., Hammond, D., Hartman, B., & Maynard, V., 1979. Early oxidation of organic matter in pelagic sediments of the eastern equatorial Atlantic: Suboxic diagenesis. Geochimica et Cosmochimica Acta, 43, 1075–1090.

Goldberg, E. D., & Arrhenius, G. O. S., 1958. Chemistry of Pacific pelagic sediments. Geochimica et Cosmochimica Acta, 13, 153–212.

Goldhammer, R.K., 1998. Second-order accommodation cycles and points of "stratigraphic turnaround": implications for carbonate buildup reservoirs in Mesozoic carbonate systems of the East Texas Salt Basin and South Texas. In: Demis, W.D., Nelis, M.K. (Eds.), West Texas Geological Society Annual Field Conference Guidebook. West Texas Geological Society Publication, vol. 98-105, pp. 11–28.

Goldhammer, R.K., and Johnson, C.A., 2001. Middle Jurrassic-Upper Cretaceous paleogeographic evolution and sequencestratigraphic framework of the northwest Gulf of Mexico rim, in C. Bartolini, R.T. Buffler, and A. Cantú-Chapa, eds., The Western Gulf of Mexico Basin: Tectonics, Sedimentary Basins, and Petroleum Systems: American Association of Petroleum Geologists Memoir 75, p. 45-81.

Hallam, A., 1978. Eustatic cycles in the Jurassic. Palaeogeography. Palaeoclimatology. Palaeoecology.23; 1–32.

Hallam, A., 1985. A review of Mesozoic climates. J. Geol. Soc. London, 142: 433-445.

Hallam, A., 1993. Jurassic climates as inferred from the sedimentary and fossil record. Philosophical Transactions of the Royal Society of London, Series B, 341, 287–296.

Hallam, A., 2001. A review of the broad pattern of Jurassic sea-level changes and their possible causes in the light of current knowledge. Palaeogeography. Palaeoclimatology. Palaeoecology. 167, 3–37.

Hammes, U., 2009. Sequence stratigraphy and core facies of the Haynesville Mudstone, east Texas: Gulf Coast Association of Geological Societies Transactions, v. 59; 321–324.

Hammes, U., Hamlin, H.S., Eastwood, R., 2010. Facies characteristics, depositional environments, and petrophysical characteristics of the Haynesville and Bossier

shale-gas plays of East Texas and northwest Louisiana. Houston Geological Society Bulletin, 59–63.

Hammes, U., Hamlin, S.H., Ewing, T., 2011. Geologic analysis of the Upper Jurassic Haynesville Shale in east Texas and west Louisiana, AAPG Bulletin, V.95, No.10; 1643–1666.

Helz, G. R., Vorlicek, T. P., Kahn, M. D., 2004. Molybdenum scavenging by iron monosulfide. Environmental Science and Technology, 38, 4263–4268.

Hesselbo, S.P., Deconinck, J-F., Huggett, J.M., Morgans-Bell, H.S., 2009. Late Jurassic palaeoclimatic change from clay mineralogy and gamma-ray spectrometry of the Kimmeridge Clay, Dorset, UK. Journal of the Geological Society, London, 166, 1123–1134.

Huerta-Diaz, M. A., & Morse, J. W., 1992. Pyritization of trace metals in anoxic marine sediments. Geochimica et Cosmochimica Acta, 56, 2681–2702.

Isaacs, C. M., 2001. Depositional framework of the Monterey Formation, California. In: C. M. Isaacs & J. Rullko¨ tter (Eds), The Monterey Formation: From rocks to molecules (pp. 1–30). New York: Columbia University Press.

Jacobs, L., Emerson, S., & Huested, S. S., 1987. Trace metal geochemistry in the Cariaco Trench. Deep Sea Research, 34, 965–981.

Kauffman, E.G., Sageman, B.B., 1990, Biological sensing of benthic environments in dark shales and related oxygen-restricted facies, In: R.N. Ginsberg and B. Beaudoin (eds.), Cretaceous Resources, Events and Rhythms: Background and plans for research , Proc. 1st Global Sedimentary Geology Program Mtng., Digne, France, NATO ASI Series C, 304, 121–138.

Klemme, H.D., 1994. Petroleum systems of the world involving Upper Jurassic source rocks. In: Magoon, L.B., Dow, W.G. (Eds.). The Petroleum System from Source to Trap. AAPG Memoir, vol. 60. pp. 51–72.

Krishnaswami, S., 1976. Authigenic transition elements in Pacific pelagic clays. Geochimica et Cosmochimica Acta, 40, 425–434.

Ku, T.-L., Knauss, K. G., & Mathieu, G. G., 1977. Uranium in the open ocean: Concentration and isotopic composition. Deep Sea Research, 24, 1005–1017.

Leckie, R.M., Bralower, T.J., Cashman, R., 2002. Oceanic anoxic events and plankton evolution: Biotic response to tectonic forcing during the mid-Cretaceous. Paleoceanography 17 (3), 1041.

Loucks, R.G., Ruppel, S.C., 2007. Mississippian Barnett Shale: Lithofacies and depositional setting of a deep-water shale gas succession in Fort Worth Basin, Texas. American Association of Petroleum Geologists Bulletin, V. 91, No. 4; 579-–601.

Mainali, P., 2011. Chemostratigraphy and the Paleoceanography of the Bossier-Haynesville Formation, East Texas Basin, Tx and La: Masters Thesis, University of Texas at Arlington.

McLean, D.C., Pharis, R.R., Goldhammer, R.K., 1999. Exploration potential and high resolution sequence stratigraphy of the Upper Jurassic Louark succession, eastern limb of the East Texas salt basin. In: Annual Meeting Expanded Abstracts, American Association of Petroleum Geologists vol A92. [p. A-xxx?]

Moore, R.W., Del Castillo, L., 1974. Tectonic evolution of the southern Gulf of Mexico: Geological Society of America Bulletin, v. 85, no. 4; 607–618.

Moore, G.T., Hayashida, D.N., Ross, C.A., Jacobson, S.R., 1992. The paleoclimate of the Kimmeridgian/Tithonian (Late Jurassic) world: I Results using a general

circulation model. Palaeogeography, Palaeoclimatology, Palaeoecology, 93: 113–150.

Moore, G.T., Barron, E.J., Hayashida, D.N., 1995. Kimmeridgian (Late Jurassic) general lithostratigraphy and source rock quality for the western Tethys Sea inferred from paleoclimate results using a general circulation model. American Association of Petroleum Geologists Studies in Geology 40, 157–173.

Murphy, A.E., Sageman, B.B., Hollander, D.J., Lyons, T.L., Brett, C.E., 2000. Black shale deposition and faunal overturn in the Devonian Appalachian Basin: clastic starvation, seasonal water column mixing, and efficient biolimiting nutrient recycling Paleoceanography 15; 280–291.

Nunn, J.A., 2012. Burial and thermal history of the Haynesville Shale: Implications for overpressure, gas generation, and natural hydrofracture. GCAGS Journal, 1:81–96.

Parrish, J.T., 1993. Climate of the supercontinent Pangea: Journal of Geology, v. 101, p. 215–233.

Piper, D. Z.,Calvert, S.E., 2009. A marine biogeochemical perspective on black shale deposition, Elsevier, Earth Science Reviews 95; 63–96.

Price, N. B., Calvert, S. E., & Jones, P. G. W., 1970. The distribution of iodine and bromine in the sediments of the southwestern Barents Sea. Journal of Marine Research, 28, 22–34.

Price, G. D., Valdes, P. J.,Sellwood, B. W., 1997. Quantitative palaeoclimate GCM validation: Late Jurassic and mid-Cretaceous case studies, Journal of the Geological Society, v. 154:769–772,doi:10.1144/gsjgs.154.5.0769.

Rees, P.M., Noto, C.R., Parrish, J.M. & Parrish, J.T., 2004. LateJurassic climates, vegetation, and dinosaur distributions. Journal of Geology, 112, 643–653.

Rimmer, S.M., 2004. Geochemical paleoredox indicators in Devonian-Mississippian black shales, Central Appalachian Basin (USA). Chemical Geology, 206; 373-391.

Rowe, H.D., Loucks, R.G., Ruppel, S.C., Rimmer, S.M., 2008. Mississippian Barnett Formation, Fort Worth Basin, Texas: Bulk geochemical inferences and Mo-TOC constraints on the severity of hydrographic restriction, Elsevier, Chemical Geology 257; 16–25.

Sageman, B.B, Murphy, A.E, Werne, J.P, Ver Straeten, C.A, Hollander, D.J., Lyons, T.W., 2003. A tale of shales: the relative roles of production in the accumulation of organic-rich strata, Middle-Upper Devonian, Appalachian basin. Chemical Geology 195; 229–273.

Sageman, B.B., Lyons, T.W., 2003. Geochemistry of fine-grained sediments and sedimentary rocks. In: MacKenzie, F. (Ed.), Treatise on Geochemistry 7. Elsevier Publishing; 115–158.

Sano J.L., Ratcliffe K.T., and Spain D.R., 2013. Chemostratigraphy of the Haynesville Shale, in U. Hammes and J. Gale, eds., Geology of the Haynesville Gas Shale in East Texas and West Louisiana, U.S.A.: AAPG Memoir 105, p. 137–154.

Schieber, J., Zimmerle, W., 1998. Introduction and overview: The history and promise of shale research, In: J. Schieber, W. Zimmerle, and P. Sethi (eds.), Shales and Mudstones I: Stuttgart, Germany, E. Schweizerhbart'sche Verlagsbuchhandlung; 1–10.

Sellwood, B. W., Valdes, P. J., 2006. Mesozoic climates: General circulation models and the rock record; Journal of Sedimentary Geology, 190(1–4):269–287.

Shaw, T. J., Gieskes, J. M., & Jahnke, R. A., 1990. Early diagenesis in differing depositional environments: The response of transition metals in pore water. Geochimica et Cosmochimica Acta, 54, 1233–1246.

Shimmield, G. B., & Pedersen, T. F., 1990. The geochemistry of reactive trace elements and halogens in hemipelagic continental margin sediments. Reviews in Aquatic Sciences, 3, 255–279.

Spain, D.R., Anderson, G. A., 2010. Controls on reservoir quality and productivity in the Haynesville Shale, Northwestern Gulf of Mexico Basin: Gulf Coast Association of Geological Societies Transactions, v. 60; 657–668.

Steinhoff, I., Cicero, A.D., Koepke, K.A., Dezelle, J., McClain, T., and Gillett, C., 2011. Understanding the regional Haynesville and Bossier shale depositional systems in East Texas and northern Louisiana: An integrated structural/stratigraphic approach: AAPG Search and Discovery Article #50379.

Taylor, S.P., Sellwood, B.W., 2002. The context of lowstand events in the Kimmeridgian (Late Jurassic) sequence stratigraphy evolution of the Wessex-Weald Basin, Southern England, Sedimentary Geology 151; 89-106.

Tribovillard, N., Abdelkader, R., Trentesaux, A., 2005. Controls on organic accumulation in Upper Jurassic Shales of Northwestern Europe as inferred from trace-metal geochemistry. In: Harris, N.B. (Ed.), The Deposition of Organic-Carbon-Rich Sediments: Models, Mechanisms, and Consequences: SEPM Special Publication, vol. 82, pp. 145–165.

Tribovillard, N., Algeo, T.J., Lyons, T., Riboulleau, A., 2006. Trace metals as paleoredox and paleoproductivity proxies: An update. Chemical Geology 232; 12–32.

Valdes, P. J., Sellwood, B. W., 1992. A palaeoclimate model for the Kimmeridgian. Paleogeography, Paleoclimatology, Paleoecology, 95, 47–72.

Van Geen, A., and HUSBY, D. M, 1996. Cadmium in the California Current system: A tracer of past and present upwelling. J. Geophys. Res. 101: 3489–3507.

Ver Straeten, C.A., Brett, C.E., Sageman, B.B., 2010. Mudrock sequence stratigraphy: A multi-proxy (sedimentological, paleobiological, geochemical) approach, Devonian Appalachian Basin; Palaeogeography, Palaeiclimatology, Palaeoecology, Vol. 204, Issue 1-2; 54–73.

Wang, F.P., Hammes, U., 2010. Effects of petrophysical factors on Haynesville fluid flow and production. World Oil, D79eD82.

Weissert, H., Erba, E., 2004. Volcanism, CO2 and palaeoclimate: A Late Jurassic-Early Cretaceous carbon and oxygen isotope record; J. Geol. Soc. London, 161, 695–702.

Werne, J.P., Sageman, B.B., Lyons, T., Hollander, D.J., 2002. An integrated assessment of a "Type Euxinic" deposit: evidence for multiple controls on black shale deposition in the Middle Devonian Oatka Creek Formation; American Journal of Science, Vol. 302, 110–143.

Williams, P., 2009. East Texas and North Louisiana have served another tantalizing reservoir the superb Haynesville shale. Oil and Gas Investor 29 (1), 50e61.

Zahm, C.K., and Enderlin M., 2010. Characterization of rock strength in Cretaceous strata along the Stuart City Trend, Texas: Gulf Coast Association of Geological Societies Transactions, v. 60, p. 693-702.

Zakharov, V. A., Baudin, F., Dzyuba, O. S., Daux, V., Zverev K. V., and Renard, M., 2005. Isotopic and faunal record of high paleotemperatures in the Kimmeridgian of Subpolar Urals. Russian Geology and Geophysics 46(1):3-20 [M. Aberhan/S. Nurnberg]